

# Matrix mechano-sensing at the invasive front induces a cytoskeletal and transcriptional memory supporting metastasis

Received: 30 October 2024

Accepted: 13 January 2025

Published online: 14 February 2025

 Check for updates

Oscar Maiques<sup>1,2,3,22</sup>, Marta C. Sallan<sup>1,4,23</sup>, Roman Laddach<sup>5,6,23</sup>, Pahini Pandya<sup>3,23</sup>, Adrian Varela<sup>1,2</sup>, Eva Crosas-Molist<sup>1,2,3</sup>, Jaume Barcelo<sup>1,2</sup>, Olivia Courbot<sup>7</sup>, Yanbo Liu<sup>1</sup>, Vittoria Graziani<sup>1,2</sup>, Youssef Arafat<sup>8</sup>, Joanne Sewell<sup>2,3</sup>, Irene Rodriguez-Hernandez<sup>2,3</sup>, Bruce Fanshawe<sup>3,9</sup>, Yaiza Jung-Garcia<sup>1,2</sup>, Paul RC Imbert<sup>10</sup>, Eloise M. Grasset<sup>11</sup>, Jean Albregues<sup>11</sup>, Maria Santacana<sup>12</sup>, Anna Macià<sup>13</sup>, Jordi Tarragona<sup>12</sup>, Xavier Matias-Guiu<sup>12,13,14</sup>, Rosa M. Marti<sup>15</sup>, Sophia Tsoka<sup>6</sup>, Cedric Gaggioli<sup>11</sup>, Jose L. Orgaz<sup>2,3,16</sup>, Gilbert O. Fruhwirth<sup>9</sup>, Fredrik Wallberg<sup>17,18</sup>, Kai Betteridge<sup>18</sup>, Constantino Carlos Reyes-Aldasoro<sup>18,19</sup>, Syed Haider<sup>20</sup>, Andrejs Braun<sup>4</sup>, Sophia N. Karagiannis<sup>5,21</sup>, Alberto Elosegui-Artola<sup>8</sup> & Victoria Sanz-Moreno<sup>1,2,3</sup>✉

The extracellular matrix (ECM) controls tumour dissemination. We characterise ECM organization in human and mouse tumours, identifying three regions: tumour body, proximal invasive front and distal invasive front. Invasive areas show increased matrix density, fibre thickness, length, and alignment, with unique radial fibre orientation at the distal invasive front correlating with amoeboid invasive features. Using patient samples and murine models, we find that metastases recapitulate ECM features of the primary tumour. Ex vivo culture of murine cancer cells isolated from the different tumour regions reveals a spatial cytoskeletal and transcriptional memory. Several in vitro models recapitulate the in vivo ECM organisation showing that increased matrix induces 3D confinement supporting Rho-ROCK-Myosin II activity, while radial orientation enhances directional invasion. Spatial transcriptomics identifies a mechano-inflammatory program associated with worse prognosis across multiple tumour types. These findings provide mechanistic insights into how ECM organization shapes local invasion and distant metastasis.

Solid tumours are characterized by heterogeneous populations of cancer cells and their tumour microenvironment (TME) composed of fibroblasts, immune cells, vessels, and the extracellular matrix (ECM)<sup>1</sup>. ECM is composed of fibrillar collagens, fibronectin, elastin, and laminins<sup>2</sup>. Aberrant ECM deposition promotes tumour cell proliferation, invasion and metastasis<sup>3</sup>. Homeostatic control of the ECM is

compromised during cancer progression, and tumour cells become exposed to a collagen-rich stroma. Besides collagen accumulation, matrix is differentially organized in pathological conditions such as cancer, aging and fibrosis<sup>4–7</sup>. Furthermore, aligned ECM fibres generate tracks for the invasion of tumour cells<sup>8,9</sup> and collagen fibre organization correlates with disease onset and progression<sup>10</sup>. Tumour-

Associated Collagen Signatures (TACS) have revealed that collagen structures differ according to location in the tumour, presenting higher levels of alignment at the tumour edge, enabling for contact guidance directed cell migration<sup>8,11,12</sup>. Nevertheless, how disseminating cancer cells sense ECM features at the invasive front and translate them into pro-metastatic signals is unclear.

Fibre alignment correlates with increased tissue stiffness and tumour cell invasion<sup>8,13,14</sup>. While sensing localised changes in substrate stiffness surrounding the cell is enabled by cell adhesions and is crucial for translating cytoskeletal forces into motion<sup>15</sup>, it is the actomyosin machinery that is responsible for the determination of overall stiffness and adoption of different migratory modes in response to varying ECM stiffness<sup>15</sup>. Moderate Myosin II activity is required for actin-rich protrusions and retraction of the cell rear, while higher Rho-ROCK-Myosin II engagement drives rounded-amoeboid migration requiring lower levels of adhesion<sup>16</sup>. Many chemical stimuli such as cytokines and growth factors support amoeboid behaviour<sup>17–21</sup>. However, physical confinement coupled to lower levels of adhesion induced fast amoeboid bleb-based migration<sup>16,22,23</sup>. Such in vitro studies led to the hypothesis that confinement imposed by surrounding tissue on a growing tumour could trigger amoeboid migration, but the mechanism by which physical confinement imposed by the matrix at the edge of tumours induces amoeboid invasion is not fully understood.

In this study, we describe three distinct ECM areas within Melanoma and Breast cancer primary tumours, each characterized by different properties that influence cancer cell cytoskeleton and behaviour. Crucially, ECM distinct organisation at these areas supports a transcriptional program in cancer cells that is important for local invasion in primary lesions and for distant metastases formation. Our findings reveal a complex interplay between ECM structure and cancer cell transcriptional responses.

## Results

### Regional characterisation of the extracellular matrix in solid tumours

We combined digital pathology and image analysis to study matrix organisation using Trichrome staining<sup>24–26</sup> and second harmonic generation (SHG)<sup>27</sup> microscopy in tissue samples. Several tissue-microarrays of tumour sections from melanoma and breast cancer (BRCA) were constructed and divided in different areas: the centre or tumour body (TB) and the invasive front (IF)-area of the tumour in contact with the matrix (Supplementary Data 1–3). Within this invasive region we could further sub-classify the matrix into two separate areas: proximal invasive front (PIF) comprising between 50–100  $\mu\text{m}$  of boundary with the extracellular matrix; and the distal invasive front (DIF) 100–200  $\mu\text{m}$  further away from the PIF (Supplementary Table 1).

QuPath<sup>24</sup> was used to assess global changes in ECM organization in the different areas (Supplementary Table 2, See methods section). In melanoma, the TB showed the lowest percentage of matrix, and this matrix was less intense and less anisotropic measured by Haralick Entropy<sup>28</sup>, while both invasive areas had much higher levels of all parameters (Fig. 1b, c). Matrix topography was assessed using curvelet transform algorithm<sup>29</sup> (Supplementary Table 2). We observed that fibres in PIF and DIF were significantly longer, thicker, straighter, showed reduced mean distance between fibres, and were more aligned compared to TB. Additionally, the fibre density of TB was significantly lower (Fig. 1d, e). Importantly, fibres were oriented parallel to the tumour boundary in the PIF while they were oriented perpendicularly or radially to the tumour border in the DIF (Fig. 1f). We next analysed matrix organization in BRCA samples and found these three separate zones with the same pattern, matrix abundance and topography we had found in melanoma (Fig. 1g–i). We validated these observations using SHG imaging and curvelet transform analysis in the same human tissue samples (Supplementary Fig. 1a–d). Collagen-I staining showed

correlation in the areas of high matrix density and high fibre alignment such as PIF and DIF, while collagen IV was only observed in the basement membranes of vessels and not in invasive regions (Supplementary Fig. 1e, f).

Overall, we observe similar regional ECM organisation in melanoma and breast cancer tissues: TB with low matrix abundance/low fibre alignment; PIF with high matrix abundance/high fibre alignment and parallel angles, and DIF with intermediate matrix abundance/high fibre alignment but perpendicular angles. Furthermore, this data shows that the key difference in the invasive areas is the orientation of the fibres at the DIF which could be steering invasive processes in cancer cells leaving the tumour mass.

### Regional organisation of ECM is associated with cytoskeletal remodelling, local invasion and metastatic spread in human tumours

We next investigated if ECM regional distribution was associated with specific invasion patterns, cytoskeletal characteristics, and metastatic spread (Supplementary Table 1). A gradual increase in circularity and pMLC2 (MLC2 activity) was observed from TB to PIF and then even further to DIF (Fig. 2a, b). Interestingly, we did not observe changes in total MLC2 levels (Fig. 2b). Both groups of cells and individual cancer cells invading were observed at PIF, but amoeboid single cell invasion was highest at the DIF which also correlated with highest invasion levels (Fig. 2c–e, Supplementary Fig. 2a).

Very similar observations were made regarding cytoskeletal changes and invasive patterns using BRCA tissues (Fig. 2f–i, Supplementary Fig. 2b), while we observed that groups of cells were larger than in melanoma. Moreover, increased amoeboid invasion correlated with higher disease stage in melanoma and lymph node engagement in breast cancer (Fig. 2k).

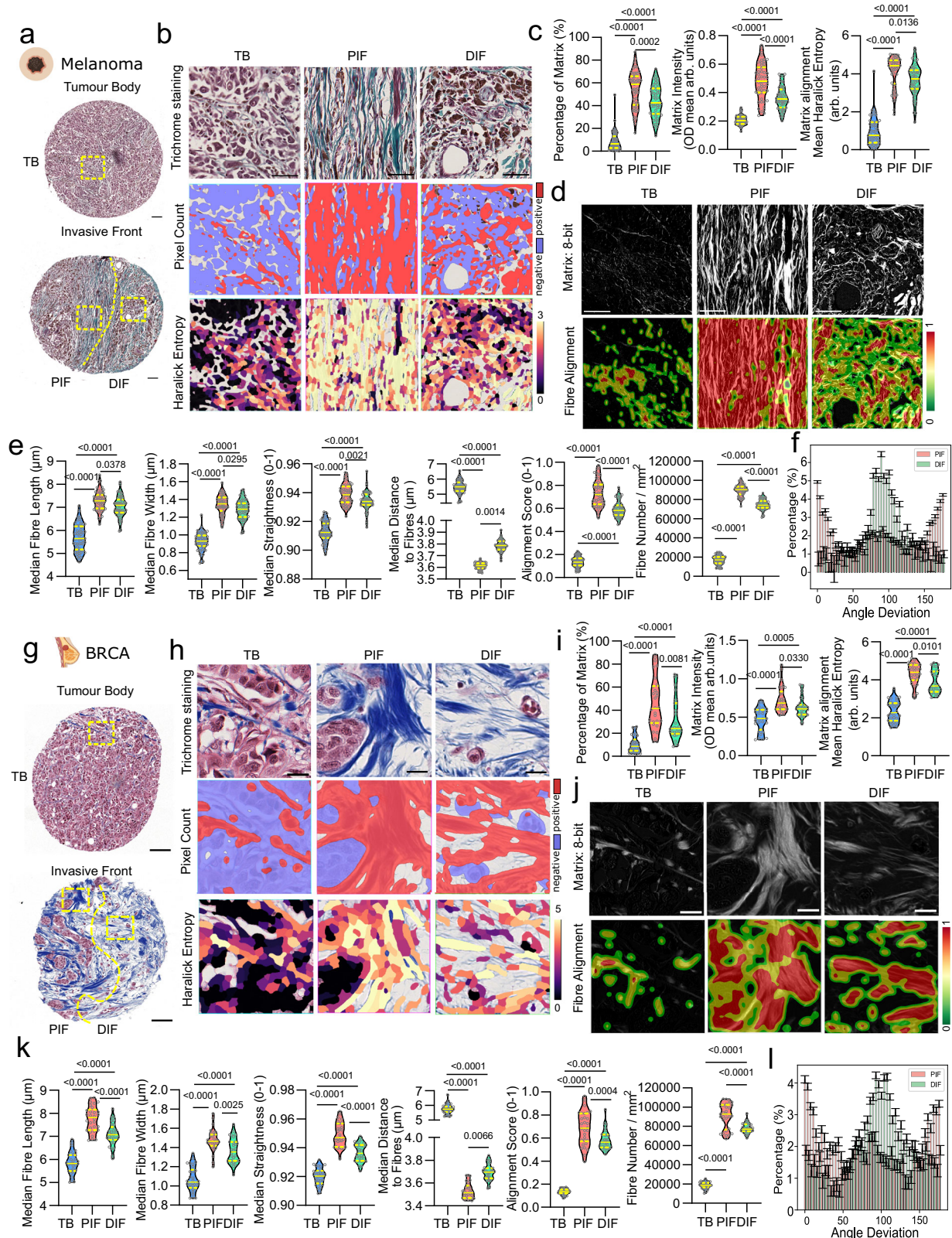
These results suggest that the three different ECM regions are associated with specific invasive patterns and cytoskeletal rearrangements in melanomas and breast cancers. Importantly the PIF to DIF area selects for amoeboid cytoskeletal characteristics that we find in association with specific matrix topographies, invasive patterns (Fig. 2l), and lymph node metastasis.

### ECM in vivo organisation is associated with a cytoskeletal memory

To study the spatial temporal relationship between matrix organisation and cytoskeletal dynamics, we used 4599 BRAF<sup>V600E</sup> mouse melanoma cells<sup>30</sup> injected ortho-topically into mouse dermis that develop lung metastasis after 30 days (both micro- and macro-metastasis) (Fig. 3a).

ECM organisation at the primary murine tumour showed a higher percentage, intensity, and alignment of matrix at the PIF and DIF compared to the TB (Fig. 3b, c). Matrix characteristics in this mouse model (Supplementary Fig. 2c) recapitulated those observed in primary human cancer tissues (Fig. 1). Importantly, similar angle orientations at DIF and PIF were observed when comparing fibres in murine tumours (Fig. 3d) to human tumours (Fig. 1f and 1l). Increased overall invasion and individual cell invasion was observed at the DIF of murine tumours (Fig. 3e) as observed in human tumours (Fig. 2).

In the metastatic tumours, we defined micro-metastasis as lesions smaller than  $-0.02\text{ mm}^2$  and found that they occupied 5–30% of metastatic lesions (Supplementary Fig. 2d). Metastasis larger than this size developed a TB and an IF and were classified as macro-metastasis. We could not detect a DIF in the macro-metastasis, likely requiring longer periods of time to invade further away. Lung micro- and macro-metastasis were characterised by different matrix characteristics (Fig. 3b, c). In macro-metastasis: there was a higher percentage of matrix at the IF, it was more intense and more aligned (Fig. 3b, c; Supplementary Fig. 2e) compared to the matrix at the TB, very much resembling the primary tumour. Importantly, micro-metastasis and the macro-metastasis IF presented similar features. We next analysed



tissues from human melanoma metastasis patients and observed similar matrix organisation patterns when compared to the primary lesions. Indeed, different regional organization was observed at the IF of metastasis compared to the TB (Supplementary Fig. 3a–d). We confirmed that fibres at the IF of metastatic lesions are longer, thicker, more compact and aligned compared to their TB (Supplementary Fig. 3a–d). These data shows that both human and mouse tumours

show matrix topographical features in the metastatic lesions that resemble those found in the primary tumour.

We then quantified the 4599 mCherry<sup>31</sup> morphology and pMLC2 and MLC2 levels in tissues derived from both the primary lesions and the lung metastasis using multiplex IHC<sup>32</sup> (Fig. 3f). We observed a gradual increase in cell rounding and pMLC2 when comparing the TB to the PIF, and then to the DIF of 4599 primary tumours (Fig. 3f, g;



**Fig. 1 | Regional organisation of the extracellular matrix in solid tumours.**

**a** TMA cores from Tumour Body (TB) and Invasive Front (IF) of primary melanoma ( $n = 53$ ), stained with Gomori trichrome. Insets show regions of interest (ROIs). Yellow lines separate proximal (PIF) and distal invasive fronts (DIF). Scale: 200  $\mu\text{m}$ . **b** ROIs from TB, PIF, DIF: trichrome staining, QuPath Pixel Count maps, Haralick Entropy alignment maps. Scale: 50  $\mu\text{m}$ . **c** Quantification of Matrix Percentage (%), Matrix Intensity (OD Mean arb. units), and Matrix Alignment (Haralick Entropy arb. units) in melanoma ( $n = 53$  patients). **d** ROIs from TB, PIF, DIF: 8-bit matrix images and CurveAlign alignment maps. Scale: 50  $\mu\text{m}$ . **e** ROI quantification: Median Fibre Length, Width, Straightness, Distance to Fibres, Alignment Score, Fibre number/ $\text{mm}^2$  ( $n = 53$  patients). **f** Angle deviation histogram comparing PIF and DIF ( $n = 53$  patients). **g** TMA cores from TB and IF of primary breast cancer (BRCA) ( $n = 30$  patients), Masson trichrome stained. Insets show ROIs. Yellow lines separate PIF

from DIF. Scale: 100  $\mu\text{m}$ . **h** BRCA ROIs: trichrome staining, QuPath Pixel Count maps, Haralick Entropy alignment maps. Scale: 20  $\mu\text{m}$ . **i** Quantification of Matrix Percentage (%), Matrix Intensity (OD Mean arb. units), and Matrix Alignment (Haralick Entropy arb. units) in BRCA ( $n = 30$  patients). **j** BRCA ROIs: 8-bit matrix images and CurveAlign alignment maps. Scale: 20  $\mu\text{m}$ . **k** BRCA ROI quantification: Median Fibre Length, Width, Straightness, Distance to Fibres, Alignment Score, Fibre number/ $\text{mm}^2$  ( $n = 30$  patients). **l** Angle deviation histogram comparing PIF and DIF in BRCA ( $n = 30$  patients). One-way ANOVA with Tukey post-hoc (c, e, i, k), displayed as truncated violin plots showing medians and quartiles. Histograms (f, l) show mean and standard error of the mean (SEM). Cartoons in Fig. 1(a, g) created in BioRender. Maiques, O. (2025) <https://BioRender.com/f02u038> <https://BioRender.com/n61t687>.

Supplementary Fig. 3f) as seen in human tumours. Circularity and pMLC2 levels were very high in micro-metastasis and at the IF of the macro-metastasis. Interestingly, TB of macro-metastasis were less rounded and with lower levels of pMLC2 and no changes in total MLC2 (Fig. 3f, g, Supplementary Fig. 3e). This data shows that this murine model can be used to study spatial-temporal dynamics of matrix and cytoskeleton both at the primary and at the metastatic site.

Next, we investigated the possibility that cells grown *ex vivo* could retain a cytoskeletal memory associated with their previous location within the tumour's heterogeneous topography. We isolated 4599 melanoma cells from the TB, PIF, and DIF in the primary tumour and from the spontaneous metastasis (MET) in the lungs. When grown on collagen *ex vivo*, we observed that melanoma cells retained the cytoskeletal features we observed in the tumours- that is increased cell rounding and pMLC2 levels in cells from the invasive areas and from the lung metastasis (Fig. 3h, i). We then grew tumour-spheroids mixing equal numbers of cells (labelled with different CellTracker dyes) extracted from the different tumour areas (cells from the TB mixed with cells from the DIF or cells from the TB mixed with cells from the MET). Both cells derived from DIF and MET out-competed cells derived from the TB in 3D invasion assays (Fig. 3j). We next argued that cells derived from the DIF- that retain cytoskeletal amoeboid features and invasive properties- are those likely to reach the vasculature and arrive to the lungs. To test if they would also survive better in the lung micro-environment, we co-injected equal numbers of TB and DIF derived cells using tail vein injection. Importantly, cells derived from DIF outperformed cells derived from the TB and survived better in the lung parenchyma after 48 h, while no difference was observed at 30 min post injection (Fig. 3k, Supplementary Fig. 3h, i). These data indicate that cancer cells extracted from the DIF retain amoeboid cytoskeletal features and pro-survival ability when they reach the lung parenchyma.

Overall, these data suggest strong associations between matrix organisation, cytoskeletal remodelling, and invasive and survival properties during metastasis.

**Collagen I accumulation induces cytoskeletal remodelling**

We next hypothesised that blocking ECM degradation *in vitro* would lead to increased local matrix density as observed in the invasive front of tumours *in vivo*. Addition of protease inhibitors (PIs) to cells grown in collagen I matrices resulted in increased length, width, straightness, and alignment of fibres, while reducing the distance between them (Fig. 4a, b) as seen *in vivo*. Both collagen I fragments and MMP activity decreased with PI treatment, indicating matrix accumulation around cells (Supplementary Fig. 4a–c). These changes in organisation led to increased matrix confinement, as shown by gap analysis (Fig. 4c). Using melanoma (4599, A375P, SKMEL28), fibrosarcoma (HT1080) and breast cancer (MDA-MB-231) cell lines, we observed an increase in amoeboid cytoskeletal features when cells grown on collagen I were treated with PI (Fig. 4d, e, Supplementary Fig. 4d–g). Moreover, 5-day organotypic assays were used to generate an invasive front and

measure invasion patterns. This approach revealed an increase in amoeboid single cell invasion after PI treatment (Supplementary Fig. 4h).

To further model *in vitro* the increase in matrix density we observe *in vivo*, we grew cancer cells in matrices containing increasing amounts of collagen I, that have been shown to display increased stiffness<sup>33,34</sup>. We found that increased collagen concentrations resulted in increased number of fibres, higher thickness of the fibres and lower distance between fibres (Fig. 4f, g), as observed in patients (Fig. 1e, k and Supplementary Fig. 1b, d). This resulted in increased matrix confinement as show by Gap analysis (Fig. 4h). On the other hand, the fibres were shorter and less aligned (Fig. 4g), which has been previously reported for high collagen containing matrices<sup>35</sup>.

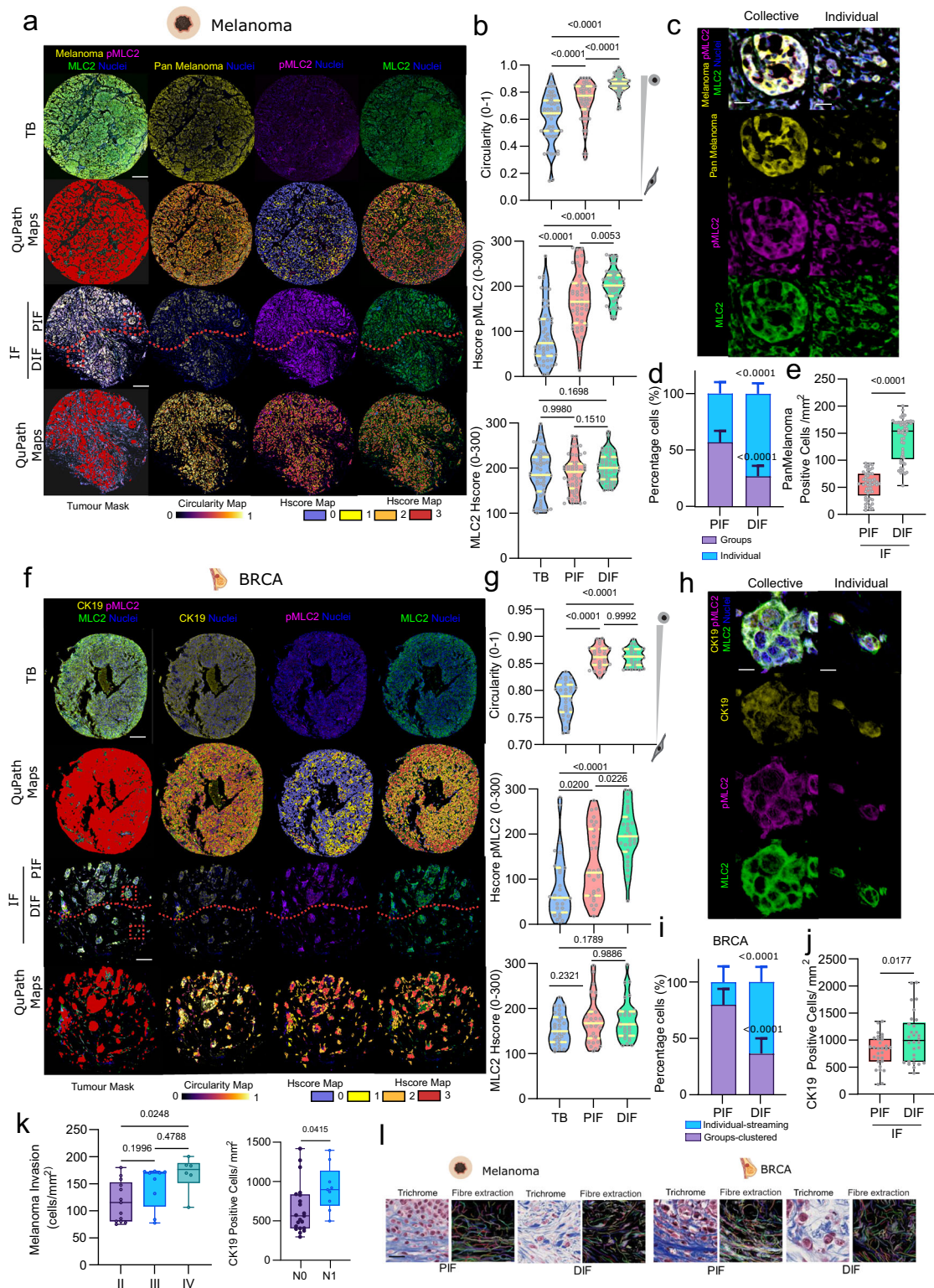
When melanoma and fibrosarcoma cancer cells were grown in increasing collagen I-containing matrices, we observed a gradual increase in cell rounding and pMLC2 levels in higher concentrations (Fig. 4i, Supplementary Fig. 4i) most likely due to the observed increased 3D confinement. Interestingly, the highest collagen concentrations resulted in decreased 3D invasion levels, likely because of shorter and less aligned fibres (Supplementary Fig. 4j).

This data supports the notion that even if matrix induced confinement increases actomyosin levels, an optimal level of collagen I supports invasion in which the fibres should be longer and more aligned.

**Collagen I accumulation and radial alignment support Myosin II driven invasive and metastatic behaviour**

Matrix alignment coupled to perpendicular fibres is a poor prognostic factor in breast cancer<sup>25</sup>. To test the hypothesis that matrix accumulation has an influence on cytoskeletal features, while the radial alignment supports maximal invasion, we used collagen gels that polymerise following Marangoni flows (Fig. 5a) driven by saturated Magnesium Chloride ( $\text{MgCl}_2$ )<sup>36</sup>. This strategy resulted in increased fibre length, thickness, straightness, density while decreasing the distance between the fibres (Fig. 5b, c, Supplementary Fig. 5a). Importantly fibres were oriented radially towards the centre of the gel (Fig. 5d), therefore recapitulating the topographical features we defined at the distal invasive front in human and mouse tissues (Figs. 1 and 3). These changes in topography also resulted in higher stiffness, as measured by atomic force microscopy (Fig. 5e). Moreover, Gap analysis revealed increased matrix confinement under these conditions (Fig. 5f). Importantly, an increase in roundness and pMLC2 levels was observed when cells were grown in the Marangoni flows-driven matrix both in 4599 and HT1080 cells, (Fig. 5h, i Supplementary Fig. 5b, c). Using tumour spheroids embedded in a collagen matrix, we observed that Marangoni flows gels favoured higher radial invasion in melanoma, fibrosarcoma and breast cancer cells (Fig. 5j, k and Supplementary Fig. 5c). This data shows that Marangoni flows-driven matrices support high actomyosin activity driven by confinement and maximal individual invasion driven by long radially oriented fibres (Supplementary Fig. 5e).





We then primed or educated cancer cells by growing them on collagen I polymerised under Marangoni flows or control matrices. After 7 days of priming on collagen I matrices, cancer cells were collected and grown in tissue culture plastic for 6 days (to test if a matrix organisation memory is retained in the absence of the matrix input). Cells derived from Marangoni-priming schedule were mixed with cells primed to control collagen, labelled with different colours and challenged to 3D invasion assays (Fig. 5n). We found that 4599 cells derived from Marangoni priming were more invasive and

retained higher pMLC2 levels (Fig. 5n-p). Importantly, when co-injecting a mix of Marangoni-primed with control-primed melanoma cells into the tail vein of mice, we found that that Marangoni priming matrix induced cytoskeletal changes that conferred a survival advantage during lung metastatic colonisation (Fig. 5q-s, Supplementary Fig. 5f).

Overall, our data indicates that matrix organisation alone can induce cytoskeletal changes that are retained over time, generating a cytoskeletal pro-invasive and pro-survival memory.

**Fig. 2 | Regional organisation of ECM is associated with cytoskeletal remodeling, local invasion and metastatic spread in human tumours.** **a** Representative multiplex images of Tumour Body (TB), Proximal Invasive Front (PIF), and Distal Invasive Front (DIF) cores in melanoma patients. Images show merged pan melanoma, pMLC2, and MLC2 markers, with individual stainings. Nuclei are stained blue. QuPath maps display tumor mask, circularity, pMLC2 H-score, and MLC2 H-score. Scale bar: 200  $\mu\text{m}$ . **b** Quantification of tumour circularity (0–1), Myosin II activity (pMLC2 H-score, 0–300), and MLC2 H-score (0–300).  $n = 53$  patients. **c** Representative images of melanoma invading cells across PIF and DIF. Scale bar: 30  $\mu\text{m}$ . **d** Percentage of individual and grouped cells invading PIF and DIF in melanoma.  $n = 53$  patients. **e** Number of invading melanoma cells/ $\text{mm}^2$  in PIF and DIF.  $n = 53$  patients per group. **f** Representative images of TB, PIF, and DIF in breast cancer (BRCA). Images show merged CK19, pMLC2, and MLC2 markers, with individual staining. QuPath maps display tumour circularity. Scale bar: 100  $\mu\text{m}$ .

**g** Quantification of tumour circularity, Myosin II activity, and MLC2 H-score in BRCA.  $n = 30$  patients. **h** Images of BRCA invading cells across PIF and DIF. Scale bar: 20  $\mu\text{m}$ . **i** Percentage of individual and grouped cells invading PIF and DIF in BRCA.  $n = 30$  patients. **j** Number of invading BRCA cells/ $\text{mm}^2$  in PIF and DIF.  $n = 30$  patients. **k** Melanoma invasion by stage (II, III, IV;  $n = 24$  patients) and BRCA invasion by lymph node status (N0, N1;  $n = 30$  patients). **l** Trichrome staining and fibre extraction in melanoma and BRCA at PIF and DIF. Scale bar: 30  $\mu\text{m}$ . One-way ANOVA with Tukey post-hoc (b, g, k) displayed as truncated violin plots. Two-way ANOVA with Tukey post-hoc (d, i), and Mann-Whitney U test (e, j). Bar graphs (d, i) show mean percentages with standard deviation error bars. Boxplots (e, j) show medians, interquartile ranges, and individual data points. Cartoons in Fig. 2(a, f, l) created in BioRender. Maiques, O. (2025) <https://BioRender.com/f02u038> <https://BioRender.com/n61t687>.

### Matrix organisation changes result in Rho-ROCK engagement and uncoupling of Myosin II from vinculin

Vinculin is required for force transmission between the matrix and the cytoskeleton<sup>37–39</sup> and is necessary for Myosin II-dependent adhesion strength and traction force<sup>40</sup>. Using super-resolution spinning disk microscopy, we analysed endogenous vinculin changes in 4599 or HT1080 cells when challenged to increasing collagen concentration or PIs. We observed that overall signal of vinculin structures decreased progressively when comparing 1.7 to 3.5 and then to 6.6 mg/ml collagen-I (Fig. 6a–c; Supplementary Fig. 6a, b) as well as overall protein levels (Fig. 6c). A drop in vinculin total levels as measured by immunofluorescence and western blot was also apparent while cancer cells where rounding-up after protease inhibition (Fig. 6d, e; Supplementary Fig. 6a, b). Furthermore, we analysed myosin light chain 2 and vinculin dynamics at actin rich protrusions. We could observe pMLC2/Vinculin signal at actin rich protrusions either in collagen 1.7 mg/ml or untreated 4599 and HT1080 cells (Fig. 6a, b, Supplementary Fig. 6a, b). However, in higher collagen concentrations (3.5, 6.6 mg/ml) or in the presence of PIs (4 h, 24 h) while protrusions had retracted and even disappeared, we observed an increase in pMLC signal vs vinculin signal in the actin cortex (Fig. 6d, e, Supplementary Fig. 6a, b). This data suggests that matrix accumulation results in uncoupling of vinculin from cell matrix adhesions/protrusions, while active MLC2 becomes cortical. Importantly, initial cell body retraction was associated with cells establishing fewer adhesions, indicated by decreased points of attachment to the matrix (Supplementary Fig. 6c). Overall, this data suggests that due to collagen I accumulation, cells respond by contracting their actomyosin cortex and lowering their matrix adhesions, uncoupling vinculin from protrusions while blebbing starts to be apparent.

RhoA is activated in response to mechanical stress<sup>41,42</sup> and, accordingly, we measured increased RhoA GTP but also RhoC GTP levels after protease inhibition (Fig. 6g). GEFH1 and LARG (ARHGEF12) are Rho GEFs that selectively activate RhoA<sup>43,44</sup> in response to applied mechanical stress<sup>41</sup>. When GEFH1 or LARG1 expression was reduced using several RNAi, cells could not change their morphology or increase Myosin II levels after protease inhibition (Supplementary Fig. 6d–f). The increase in Myosin II levels was ROCK dependent, as shown using ROCKi, H152 (Fig. 6h, i).

These results suggest that upon inhibition of peri-cellular proteolysis, changes in matrix organisation led to RhoGEF/RhoA/C/ROCK/MLC2 activation. After Myosin II is uncoupled from vinculin-based adhesions, high RhoA/C-ROCK activity results in Myosin II strongly localising to the cortex, cells lowering adhesion levels with a clear induction of amoeboid blebbing behaviour.

### Matrix organisation drives a pro-metastatic transcriptional program

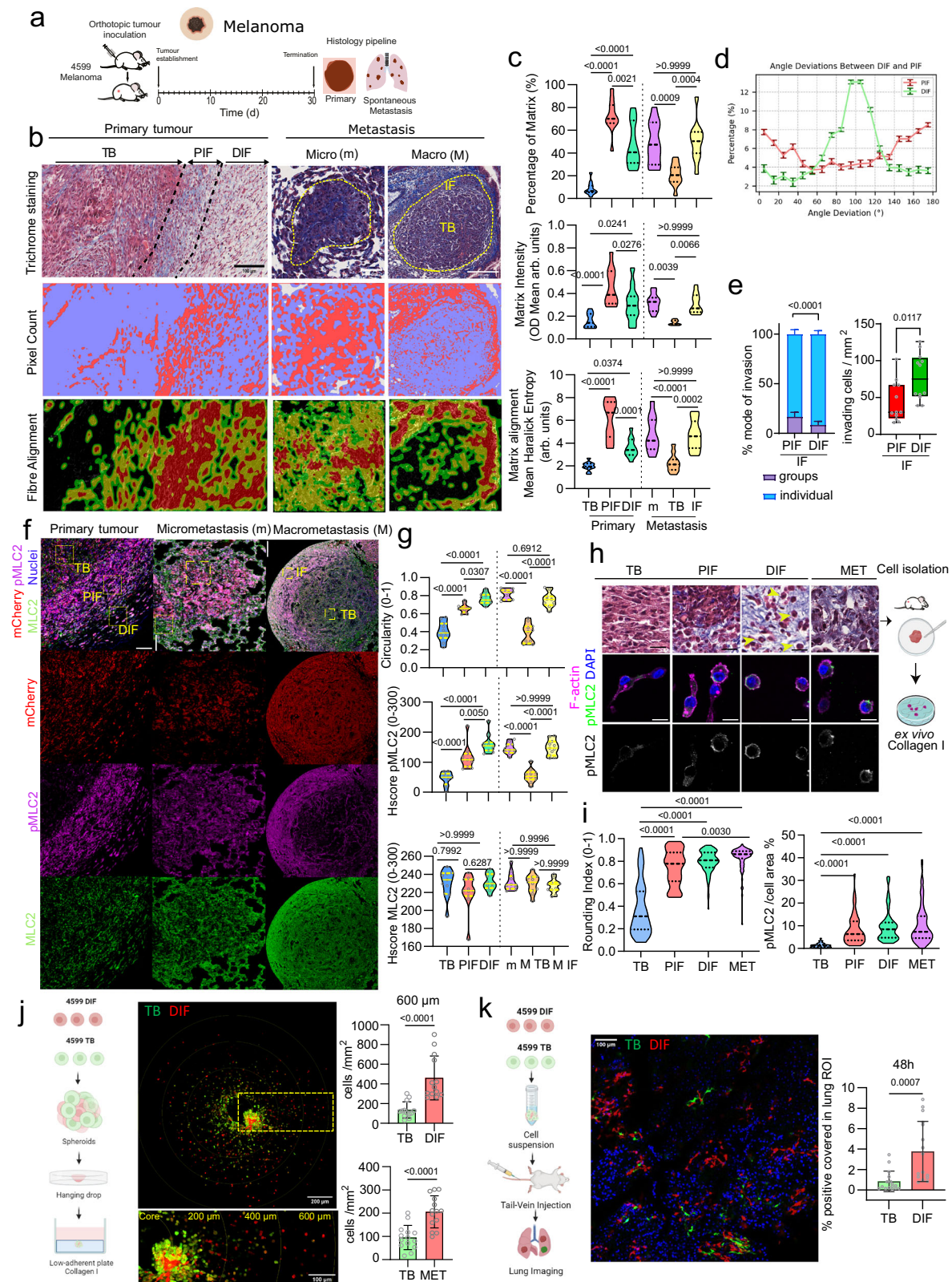
To understand if cytoskeletal changes linked to matrix organisation were coupled to a specific transcriptional program, we performed

RNA sequencing on 4599 melanoma cells, which were extracted from the three distinct regions of the primary tumour (TB, PIF, and DIF) and the lung metastasis (MET) (Fig. 7a). Unsupervised PCA plot showed four separate clusters corresponding to each region (Fig. 7b). Gene overrepresentation analysis showed 4 major gene categories that were increased and shared by cells derived from PIF and DIF compared to the TB. We observed enrichment in genes related to ECM remodelling in cancer cells derived from either PIF, DIF or MET compared to cells derived from the TB (Fig. 7c). Interestingly, cancer cells derived from PIF, were enriched in genes encoding for matrix metalloproteases (Supplementary Fig. 7a), while cells extracted from DIF areas expressed higher levels of collagen encoding genes and collagen crosslinking enzymes (Supplementary Fig. 7a). Importantly, both collagen and LOX genes were sustained in cancer cells extracted from metastatic lesions (Supplementary Fig. 7a).

RNAseq analysis showed that PIF, DIF and MET derived cells shared gene expression programmes related to mechano-sensing, cell migration, GTPase activity, amoeboid type migration, chemotaxis, and angiogenesis (Fig. 7c). Such processes were enriched progressively in cells derived from PIF to cells derived from DIF and then to cells derived from MET (Fig. 7c). Transcription factor (TF) analysis based on differential expression genes showed that TEAD4 – a major regulator of YAP mechano-sensing – was enriched in PIF derived cells compared to TB derived cells (Fig. 7d, Supplementary Fig. 7b). STAT3 and inflammation/survival related genes and EMT master regulators (Snail, Twist1) were enriched in DIF derived cells (Fig. 7d). Further GSEA analysis showed gene upregulation of inflammatory response (Hallmark) in PIF, DIF and MET derived cells when compared to TB derived cells (Fig. 7e). Given that NF- $\kappa$ B, STAT, TGF- $\beta$  and Interferon signatures were significantly upregulated (Fig. 7e), increased YAP levels, and NF- $\kappa$ B and STAT3 activity were confirmed at protein level in cancer cells extracted from the different areas and grown in collagen ex vivo (Fig. 7f).

Transcriptomic analysis of HT1080 cells treated with protease inhibitors showed similar gene expression changes that were also related to the HIPPO/YAP and NF- $\kappa$ B pathways after 4 h, and an enrichment in survival, inflammation, and metabolism related genes, including JAK-STAT3, PI3K, P38-MAPK, after 24 hours (Supplementary Fig. 7c, d). We confirmed that using all the 3 models: increasing collagen concentrations, Marangoni flows and protease inhibitors induced a similar mechano-inflammatory response in vitro (Fig. 7g, h, Supplementary Fig. 7e–g), suggesting that this is a response to the increased physical confinement induced by the 3 models. Furthermore, priming melanoma cells to Marangoni flow-induced matrices for 7 days and removing the priming for 6 days resulted in a persistent activation of STAT3 activity (pSTAT3) (Fig. 7i). Moreover, we confirmed that knockdown of either YAP or NF- $\kappa$ B in the presence of PIs impaired the activation of STAT3 (Fig. 7j) while RNAi knockdown of YAP, NF- $\kappa$ B, and STAT3 impaired cytoskeletal remodelling after PI





treatment, indicating their cooperation in matrix organisation-induced responses (Fig. 7k).

Finally, in tissue sections from mouse primary tumours and lung metastases, progressive increases in nuclear YAP, p65, and pSTAT3 were observed from TB to PIF and to DIF (Fig. 7l, m, Supplementary Fig. 7h). Micro-metastases and macro-metastases showed distinct

expression patterns. High levels of the 3 markers were found in micro-metastases and higher levels were found at the border of macro-metastases compared to the tumour bodies of the same lesions (Fig. 7l, m, Supplementary Fig. 7h).

Overall, these results indicate that different transcriptional programs are spatially activated in tumours in response to ECM changes.



**Fig. 3 | ECM in vivo organisation is associated with a cytoskeletal memory.**

**a** Diagram showing 4599 mouse melanoma orthotopic model. Intradermal cancer cell injection leads to development of primary tumours and spontaneous lung metastasis. **b** Histological images of primary tumour (TB, PIF, DIF) and metastasis (micro/macro) showing trichrome staining, QuPath intensity map, and CurveAlign fibre alignment. Scale bars: 100  $\mu$ m (primary), 50  $\mu$ m (micro), 200  $\mu$ m (macro). **c** Quantification of Matrix Percentage (%), Matrix Intensity (OD Mean arb. units), and Matrix Alignment (Haralick Entropy arb. units).  $n = 11$  mice. **d** Angle deviation line plot comparing PIF (red) and DIF (green) fibre distributions.  $n = 11$  mice. **e** Quantification of individual versus grouped cell invasion at PIF/DIF, and invading cells/mm<sup>2</sup> count.  $n = 11$  mice. **f** Multiplex images of primary tumour and metastases showing merged and individual channels (mCherry, pMLC2, MLC2). Nuclei in blue. Scale bars: 100  $\mu$ m (primary), 20  $\mu$ m (micro), 300  $\mu$ m (macro). **g** Quantification of tumour circularity (0–1), pMLC2 H-score (0–300), and MLC2 H-score (0–300).  $n = 11$  mice. **h** Ex vivo analysis of cells isolated from TB, PIF, DIF and metastasis in Collagen

I, showing F-actin and pMLC2 staining. Nuclei in blue. **i** Quantification of cell rounding index and pMLC2/cell area from ex vivo isolates.  $n = 100, 76, 90$  and  $90$  cells per group, 3 independent experiments. **j** Spheroid invasion assay comparing TB (green) and DIF (red) cells and TB (green) and Met (red), with quantification at 600  $\mu$ m from core. Scale bars: 200  $\mu$ m, inset 100  $\mu$ m.  $n = 13$  and 14 spheroids per group. **k** Lung colonisation assay showing TB (green) versus DIF (red) cells in lung colonization. Nuclei in blue.  $n = 16$  mice. One-way ANOVA with Šidák (c, g) and Tukey post-hoc (i) displayed as truncated violin plots showing medians and quartiles. Unpaired *t*-test (e right, j, k) shown as bar graphs with mean  $\pm$  SD (e left, j) and boxplots showing median, interquartile range and individual data points (e right). Two-way ANOVA with Sidak post-hoc (e left). Angle deviation data (d) presented as line plot with SEM error bars. Cartoons in Fig. 3 (a, h, j, k) created in BioRender. Maiques, O. (2025) <https://BioRender.com/z35l297> <https://BioRender.com/f02u038>.

These programs, initially triggered by matrix organisation, are perpetuated through pro-inflammatory and pro-survival signalling pathways during the metastatic cascade.

### Matrix organisation induced transcriptional program in human tumours correlates with worse outcome

We sought to validate our results in the human clinical setting. We combined the signatures derived from collagen in vitro models and the signature derived from cells purified from DIF areas in vivo and we obtained a list of 325 genes that we defined this as “Mechano-Inflammatory Signature” (MIS) in which STAT3, TGF- $\beta$  and cytoskeletal genes were present (Fig. 8a, Supplementary Fig. 8a, Supplementary Data 4). Using spatial transcriptomics in human melanoma metastasis lesions, we annotated IF and TB in situ, while we observed that MIS was upregulated at the IF (Fig. 8a, b, Supplementary Fig. 8b). Importantly, differential gene expression from IF compared to TB showed an enrichment for ECM components (Collagens, Fibronectin, MMPs) together with STAT and NF- $\kappa$ B genes (Fig. 8c). Furthermore, we validated that Gene-Ontology signatures related to MIS were activated at the IF compared to TB (Fig. 8d).

Finally, we confirmed in TMAs of human primary melanomas that nuclear YAP1, p65 and pSTAT3 levels were enriched in cancer cells at the PIF compared to the TB, while cells at the DIF of the primary lesions had the highest levels (Fig. 8e, f). Moreover, cells at the IF of human melanoma metastasis were also enriched for YAP-p65-pSTAT3 compared to the TB (Fig. 8e, f; Supplementary Fig. 8c). Metastasis confers worse prognosis to patients<sup>45</sup>, therefore we hypothesized that the IF of primary tumours could already harbour prognostic information if cancer cells retain the matrix organisation-induced transcriptional program later in metastasis. Indeed, DIFs with higher presence of triple positive (YAP1-p65-pSTAT3) cancer cells ( $> 150$  cells/mm<sup>2</sup>) were associated with shorter melanoma patient survival (Fig. 8g). Moreover, higher fibre alignment at the DIF was also associated with shorter melanoma patient survival (Fig. 8g). Importantly, using transcriptomics data from TCGA (UVM, PDAC, HNSC, LIHC, SKCM, KIRP, CESC, LUAD, LGG, MESO, KIRP, LUSC, BLCA, GBM) and METABRIC (BRCA) especially in TNBC, we found that MIS is associated with shorter survival in several solid tumour types (Supplementary Fig. 9a, b).

This data shows that matrix organisation at the edge of primary tumours supports cytoskeletal remodelling and a transcriptional program that is conserved in metastatic lesions (Fig. 9) and is associated with worse prognosis.

### Discussion

High collagen expression and deposition have been correlated with poor patient survival<sup>46,47</sup>. Increased collagen poses a challenge that can limit cancer cell invasion<sup>1</sup> while aligned matrix fibres facilitate invasion<sup>1,13</sup>. We use digital pathology, second harmonic generation,

and curvelet transform methods to analyse ECM organisation, cancer cell cytoskeletal remodelling, and transcriptional reprogramming. We find that human tumours are characterized by 3 different regions in terms of 1) distance to the tumour centre, and 2) matrix deposition, alignment, and fibre orientation: TB, PIF, and DIF. We observe that increased matrix deposition (linked to increased physical confinement) can promote cell body retraction resulting in amoeboid cell features as observed at the PIF and DIF. Importantly, aligned radial/perpendicular orientation of the fibres away from the TB is conducive of maximal amoeboid invasion.

Our work builds upon seminal observations by Provenzano and colleagues that found how high fibre alignment, coupled with perpendicular fibre orientation was associated with poor patient prognosis in BRCA<sup>9,10</sup>. In the current work, we go further to define spatially matrix organisation: PIF areas which share features described as TACS2, while DIF areas share features with TACS3. Moreover, we expand the characterisation of the regional matrix architecture in primary and secondary tumours in two clinical models of invasive and metastatic tumour types (melanoma and breast cancer), while we explain how cytoskeletal remodelling coupled to transcriptional reprogramming is crucial for local invasion and metastatic colonisation.

To model collagen accumulation in vitro, we built gels containing increasing collagen concentration and/or gels that accumulated uncleaved collagen by blocking matrix metallo-protease activity. To specifically recapitulate the DIF, we used Marangoni flows as a method to polymerise collagen fibres radially<sup>36</sup>. We observe that directionality of the radial fibres is also coupled to increased thickness, length, and alignment of fibres. Importantly, using tumour-spheroid invasive assays, we measure increased rounded amoeboid directed invasion when the fibres are oriented in a radial fashion.

Numerous studies have explored how ECM biomechanical properties like stiffness, confinement, and viscoelasticity affect tumour progression<sup>48–52</sup>. In the current study, we find that collagen accumulation after blocking proteases or increasing its concentration (and its stiffness) results in cell individualisation and cell contraction/rounding due to increased 3D confinement. Protease inhibition leads to a switch in the mode of migration to amoeboid strategies, while very high collagen concentration will lead to overall less invasion (but remaining invasion will be individual amoeboid). Importantly, using Marangoni flows that recapitulate all the conditions seen in vivo at the DIF: more fibres, thicker and longer fibres that are closer to each other and are both straighter and more aligned. We then observe: 1. an increase in actomyosin contractility and 2. optimal directed migration. In summary, increasing collagen I around the cells via increasing its concentration, blocking proteases or using Marangoni flows will result in cell body retraction, cell rounding and increased actomyosin contractility due to the increased confinement. However, it is the radial alignment of the longer fibres that supports higher migratory and invasive behaviour (Fig. 5j, Supplementary Fig. 5d). Importantly, we

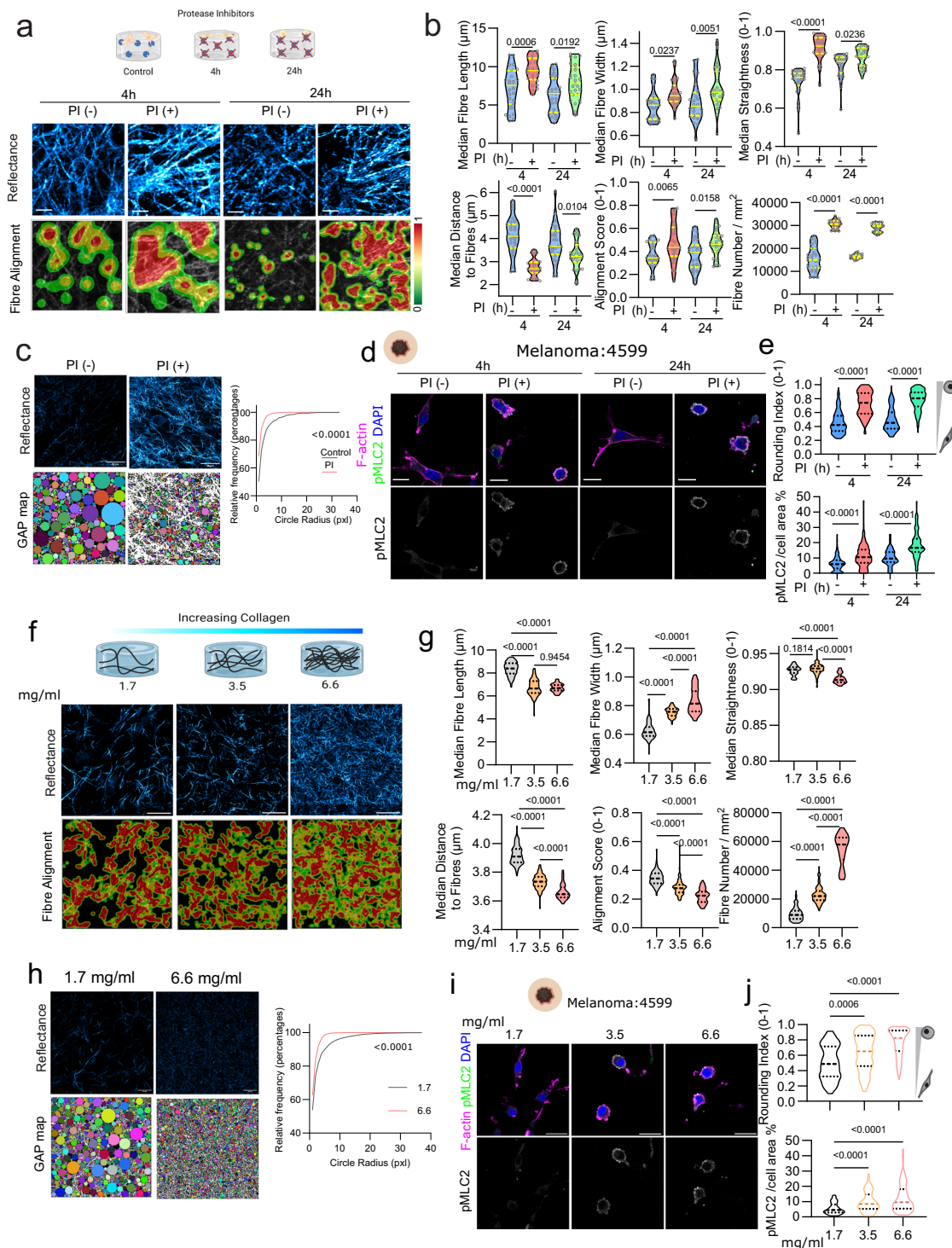
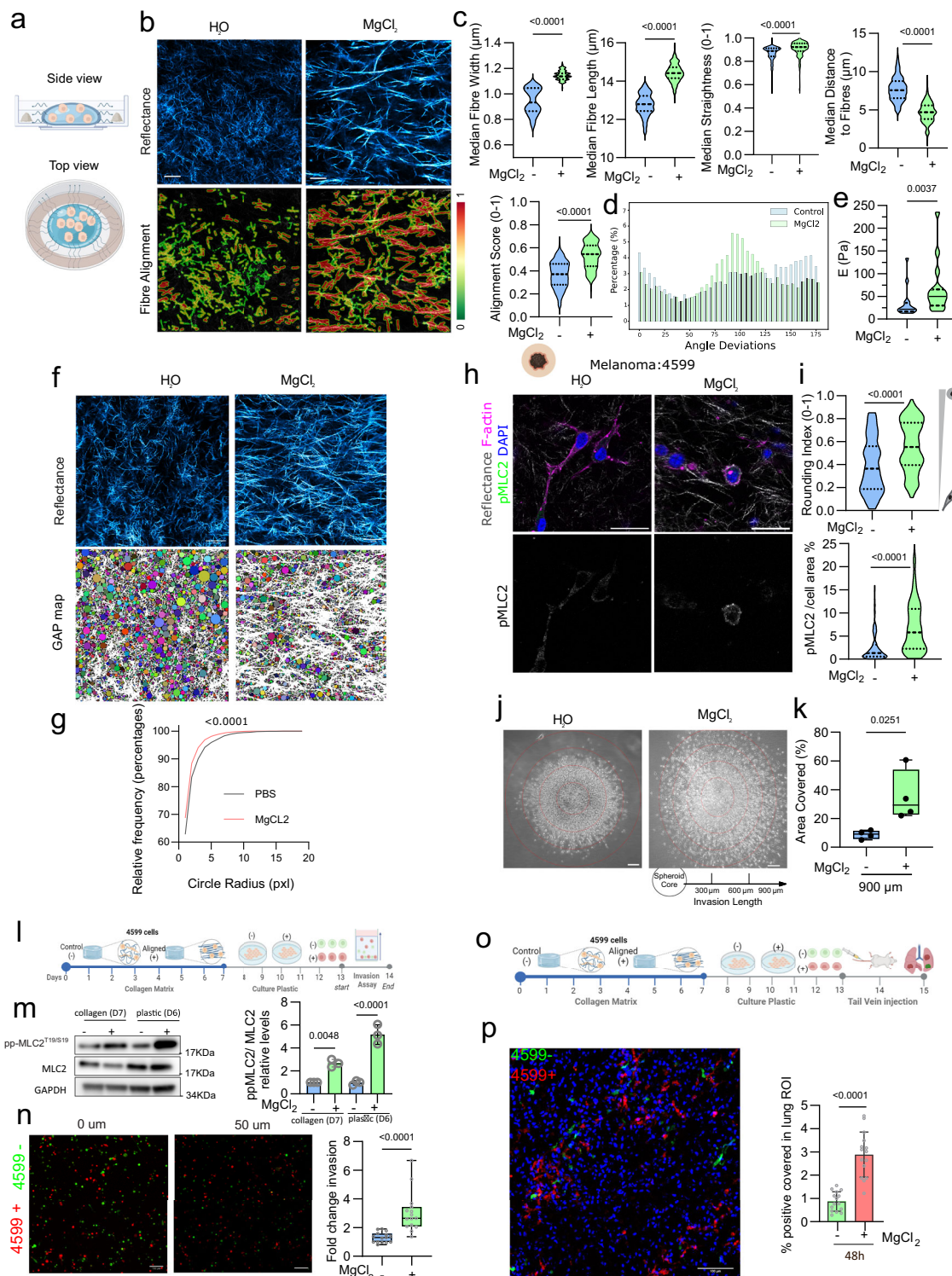


**Fig. 4 | Collagen I accumulation induces cytoskeletal remodelling. a** Experimental setup showing protease inhibitor (PI) treatment of cells in a collagen I matrix. Images show collagen reflectance and CurveAlign matrix alignment maps at 4 h and 24 h. Scale bar: 5  $\mu$ m. **b** Matrix analysis quantifying fibre length, width, straightness, distance, alignment score, and fibre number/mm<sup>2</sup> with/without PI at 4 h and 24 h.  $n = 27, 25, 26$  and 27 samples analysed from three independent experiments. Sidak one way. **c** Collagen reflectance images with gap analysis map and quantification comparing control versus PI treatment.  $n = 1066$  and 2052 gaps analysed, three independent experiments. Scale bar: 20  $\mu$ m. **d** Immunofluorescence of F-actin (magenta) and pMLC2 (green) in 4599 cells  $\pm$  PI. Nuclei in blue. Scale bar: 10  $\mu$ m. **e** Quantification of cell rounding index and pMLC2/cell area.  $n = 134, 155, 122$  and 155 cells from three independent experiments. **f** Collagen images at increasing concentrations (1.7, 3.5, 6.6 mg/mL) by confocal reflectance microscopy. Scale bar:

20  $\mu$ m. **g** Matrix analysis quantifying fibre length, width, straightness, distance, alignment score, and fibre number/mm<sup>2</sup> at increasing concentrations (1.7, 3.5, 6.6 mg/mL).  $n = 90, 78$  and 55 images, three independent experiments. **h** Collagen reflectance images with gap analysis comparing 1.7 and 6.6 mg/mL collagen.  $n = 3584$  and 10493 gaps analysed, three independent experiments. Scale bar: 20  $\mu$ m. **i** Immunofluorescence showing F-actin and pMLC2 in 4599 cells at different collagen concentrations. Nuclei in blue. **j** Quantification of rounding index and pMLC2/cell area across collagen concentrations.  $n = 110, 95, 151$  cells, three independent experiments. One-way ANOVA with Sidak (b, e) and Tukey post-hoc (g, j) displayed as violin plots showing medians and quartiles. Mann-Whitney U test between (c, h) shown as cumulative plots. Cartoons in Fig. 4(a, d, f, i) created with BioRender Maiques, O. (2025) <https://BioRender.com/z57v040> <https://BioRender.com/f02u038>.



link matrix organisation to cellular decisions in different time scales: cytoskeletal dynamics (short term) and transcriptional reprogramming (long term).

Even if we have focussed our efforts on collagen I matrix organization, the ECM is a complex network where other fibrillar proteins, such as fibronectin, laminins, or other collagens, could play a role. Data obtained from RNAseq approaches in cells extracted from different mouse tumour areas and the spatial transcriptomics performed in human tissues reveals that cancer cells produce other collagens (see Supplementary Data 4). Importantly, our RNA-seq analysis showed

that different pathways associated with ECM remodelling are activated or downregulated depending on the location within the tumour (Supplementary Fig. 7a). We provide evidence that cells in the PIF region upregulate MMP/TIMP genes, while cells in the DIF region upregulate collagen genes and the lysyl oxidase (LOX) genes. Future work should focus on understanding the role of other fibrillar proteins together with collagen I in controlling the cytoskeletal and transcriptional memory we describe in our studies.

Furthermore, our work highlights the complexity of cell-ECM interactions and the importance of considering the dimensional



**Fig. 5 | Collagen I accumulation and radial alignment support Myosin II driven invasive and metastatic behaviour.** **a** Schematic showing how  $\text{MgCl}_2$  affects collagen matrix alignment, illustrated in side and top views. **b** Collagen reflectance images comparing  $\text{H}_2\text{O}$  and  $\text{MgCl}_2$  treatment, showing reflectance and CurveAlign matrix alignment maps. Scale bar: 20  $\mu\text{m}$ . **c** Matrix analysis quantifying fibre parameters (length, width, straightness, distance, alignment score, fibre number/ $\text{mm}^2$ ).  $n = 150$  and 132 images, three independent experiments. **d** Angle deviation histogram comparing control versus  $\text{MgCl}_2$ -treated collagen fibres ( $n = 30$  samples per group). **e** AFM elasticity (Pa) measurements of control and  $\text{MgCl}_2$ -treated collagen.  $n = 15$  per group, two independent experiments. **f** Reflectance images with gap analysis maps. Scale bar: 20  $\mu\text{m}$ . **g** Gap analysis quantification comparing control and  $\text{MgCl}_2$  collagen fibres.  $n = 6941$  and 6125 gaps analysed, three independent experiments. **h** Immunofluorescence of F-actin (magenta) and pMLC2 (green) in 4599 cells  $\pm \text{MgCl}_2$ . Nuclei in blue. Scale bar: 20  $\mu\text{m}$ . **i** Cell rounding index and pMLC2/cell area quantification in 4599 cells  $\pm \text{MgCl}_2$ .  $n = 140$  and 160 cells, three independent experiments. **j** Spheroid assay showing 4599 cell invasion length in non-aligned ( $\text{H}_2\text{O}$ ) /aligned ( $\text{MgCl}_2$ ) matrices. Scale bar: 200  $\mu\text{m}$ . **k** Area coverage

quantification from 4599 tumour spheroids at 900  $\mu\text{m}$  from spheroid core comparing non-aligned ( $\text{H}_2\text{O}$ ) /aligned ( $\text{MgCl}_2$ ) matrices.  $n = 4$  independent experiments. **l** Diagram of 3D invasion assay schematic using educated 4599 cells in non-aligned ( $\text{H}_2\text{O}$ ) /aligned ( $\text{MgCl}_2$ ) matrices. **m** Western blot of ppMLC2 and MLC2 in primed cells.  $n = 3$  independent experiments. The samples derive from the same experiment but different gels for pp-MLC2<sup>T19/S19</sup> and GAPDH, and another for MLC2 were processed in parallel. **n** 3D invasion images at 0  $\mu\text{m}$  and 50  $\mu\text{m}$  with quantification. Scale bar: 100  $\mu\text{m}$ .  $n = 3$  independent experiments. **o** Diagram of in vivo lung invasion assay schematic using pre-educated 4599 cells. **p** Lung parenchyma representative image at 48 h post-injection. Scale bar: 100  $\mu\text{m}$ . ROI quantification at 30 min and 48 h.  $n = 14$  mice, 2 independent experiments. Unpaired t-test (c, i, k, n) and Mann Whitney test (e, f) between  $-/+$  conditions. One-way ANOVA with Šidák post-hoc test (m). Data is displayed as violin plots showing individual data points and medians (c, e, i), boxplots showing median, interquartile range and individual data points (k, n), Bar plot with Mean and SD (m, p), and histogram in (d). Cartoons in Fig. 5(a, h, l, o) created in BioRender. Maiques, O. (2025) <https://BioRender.com/z35l297>.

context when investigating cell motility and adhesion mechanisms. In agreement with previous work, we show that vinculin dynamics and protein levels can change when cells are under confinement, leading to the loss of strong cell-ECM adhesions<sup>53,54</sup>. Furthermore, we find that the initial changes in matrix organization result in the activation of the RhoA/C-ROCK-Myosin II pathway, leading to cytoskeletal contraction<sup>11,55,56</sup>.

On the other hand, melanoma cells isolated from the TB, PIF, DIF, and MET retained actomyosin contractility levels *ex vivo* and this correlated with their invasive and pro-survival properties. Transcriptomic analysis showed that ECM remodelling, mechano-sensing, pro-survival/pro-inflammatory and cytoskeleton organization-related genes, were all enriched in the cells derived from the invasive areas and the metastatic lesions. We find that matrix organisation-induced responses are linked to YAP-NF- $\kappa\text{B}$  activation, while STAT3 signalling sustains cytoskeletal features of amoeboid migration in the long term. STAT3<sup>37,57</sup> and NF- $\kappa\text{B}$ <sup>58</sup> regulate Myosin II activity via cytokines such as IL-6/LIF or IL-1 $\alpha$ . However, in the current work, we propose that matrix organisation on its own leads to the activation of these signalling pathways, independently of such biochemical signals. Mechanistically, we show that collagen polymerised using Marangoni flows alone can prime cells for invasion and lung colonisation via Myosin II (pro-invasive) and pSTAT3 (pro-survival) activation. These findings suggest that biophysical adaptations induced by collagen mechanosensing are retained throughout the metastatic process via acquisition of a mechanical memory. From our bioinformatic analysis, we can speculate that such memory could be supported by epigenetic factors such as npBAF<sup>59</sup> complex or ARID1A<sup>60</sup>, as we find expression levels are increased in the invasive areas (Fig. 7d, Supplementary Fig. 7b). Other types of biophysical adaptations supporting metastasis have been reported, which together with the current work highlight the importance of the physical properties of the micro-environment during cancer progression and metastasis<sup>61</sup>.

In conclusion, this work clarifies how physical coupling/uncoupling of the cytoskeleton from the matrix leads to long-term molecular events that sustain efficient metastatic dissemination. Our observations suggest that matrix organisation, cytoskeletal features and transcriptional activation are strong predictors of aggressive behaviour of cancer cells. Patients with these tumour architectures could benefit from therapies targeting these pro-invasive and pro-survival programs linked to collagen dynamics. For example, pan-LOX inhibitors are under active preclinical investigation for highly desmoplastic tumour types, thus PXS-5505 is a strong candidate in future clinical trials<sup>62–64</sup>. Furthermore, YAP1 (NCT04590664) or JAK1<sup>65</sup> inhibitors are currently being tested in preclinical and clinical studies to treat cancer. We have used cancer as a model, but our work will shed light on other physiological conditions in which matrix organisation could influence

cell migration and cell survival, such as during development, fibrosis, aging, wound healing, and immune responses.

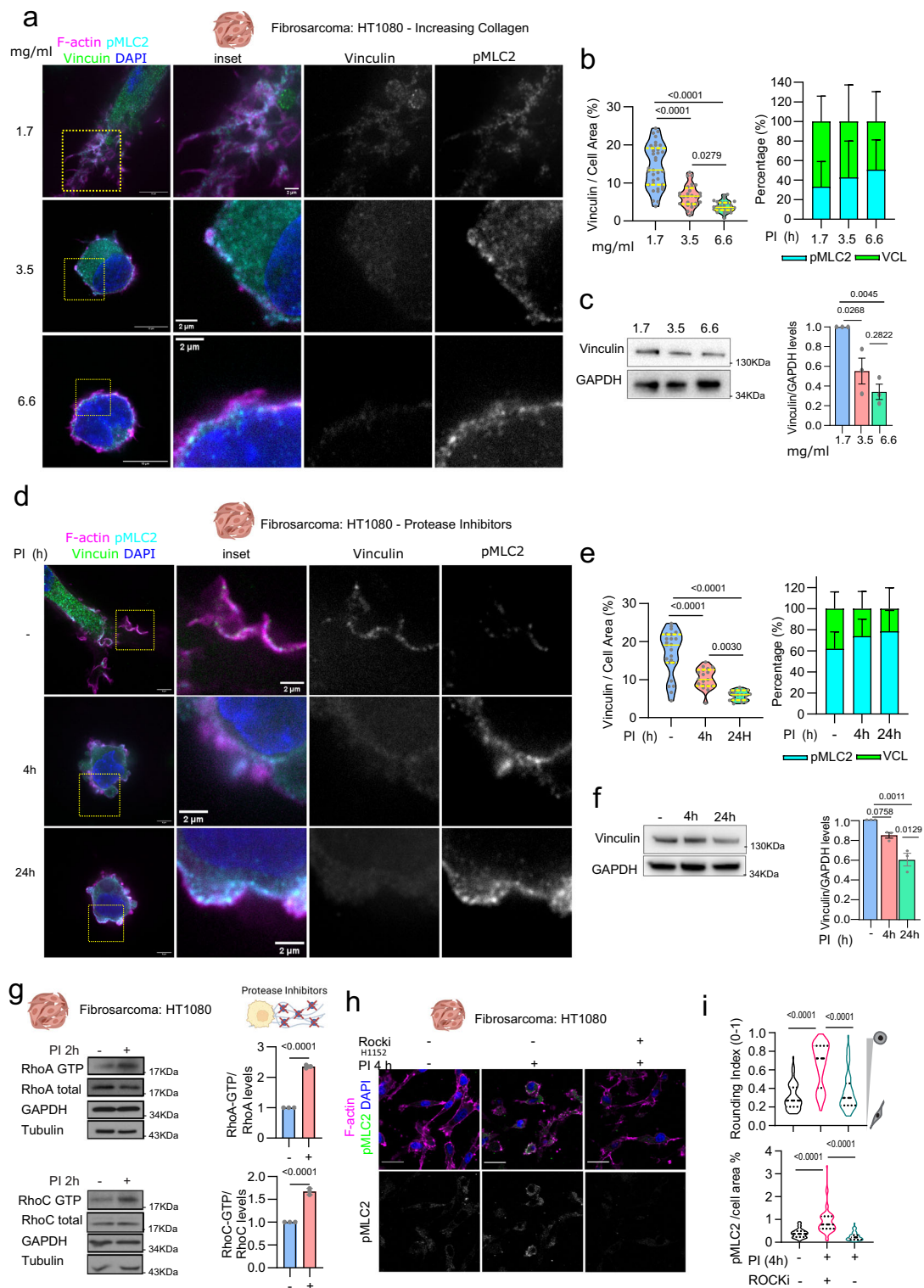
## Methods

### Compliance

This research complies with all relevant ethical regulations; all animals were maintained under specific-pathogen-free conditions and handled in accordance with the Institutional Committees on Animal Welfare of the UK Home Office (The Home Office Animals Scientific Procedures Act, 1986). All animal experiments were approved by the Ethical Review Process Committees at Barts Cancer Institute or King's College London and carried out under license from the Home Office, UK. For human tumour material, tumour samples were processed by IRB Lleida (PT17/0015/0027) and HUB-ICO-IDIBELL (PT17/0015/0024) Biobanks integrated in the Spanish National Biobank Network and Xarxa de Bancs de Tumors de Catalunya following standard operating procedures with approval of their ethics and scientific committee and were collected with specific informed consent, in accordance with the Helsinki Declaration. Consent to report patient data has been obtained and it is included in the study's ethical compliance. Compensation was not provided. This study did not specifically account for sex or gender in the experimental design because the samples were obtained as part of routine clinical practice or were retrospectively collected from existing repositories. Thus, participant recruitment was not influenced by sex or gender.

### Antibodies and inhibitors

Antibodies and dilutions used: pSer19-MLC2 (#3671, immunofluorescence, 1:200; immunohistochemistry, 1:100), pThr18/Ser19-MLC2 (#3674, immunoblotting, 1:750), MLC2 (#3672, immunoblotting, 1:750), MLC2[D18E2] (#8505, Immunohistochemistry, 1:300), pY705-STAT3 (#9145, immunoblotting, 1:750; immunohistochemistry, 1:100), NF- $\kappa\text{B}$ 1 (#4764; immunoblotting, 1:500), RhoA [67B9] (#2117, immunoblotting, 1:750), RhoC[D40E4] (#3430, immunoblotting, 1:750), STAT3[124H6] (#9139, immunoblotting, 1:750), p65[C22B4] (#4764, immunoblotting, 1:750; immunohistochemistry, 1:200), pSer536-p65 (#3036, immunoblotting, 1:750) from Cell Signalling Technology; LARG (sc-25638; immunoblotting, 1:500), YAP1 (sc-101199, immunohistochemistry, 1:100, immunoblotting, 1:750) from Santa Cruz Biotechnology; GAPDH (MAB374; 1:10,000) from Millipore; Melanoma antibody [HMB45 + M2-7C10 + M2-9E3 + T311] (ab733; immunohistochemistry, 1:300), Cytokeratin-19 [EP1580Y] (ab52625, immunohistochemistry, 1:500); Vinculin (V9131; immunofluorescence, 1:200, immunoblotting, 1:5000) from Sigma; GEF-H1 (ab90783; immunoblotting, 1:500) from Abcam; affinity-purified antibody COL1- $\frac{3}{4}\text{C}$  (no. 0217-050, immunofluorescence; 1:200) directed against the C-terminal cleavage neo-epitope of collagen types I and II, Collagen I



(ab34710; immunohistochemistry, 1:1000), Collagen IV (M0785; Immunohistochemistry; 1:25) from Agilent.

Protease inhibitor mix: 100  $\mu$ M GM6001, 50  $\mu$ M Pepstatin A, 250  $\mu$ M E64, 2  $\mu$ M Aprotinin, 2  $\mu$ M Leupeptin. GM6001 and H1152 were from Merck Millipore (Hertfordshire, UK); Pepstatin, E-64, Aprotinin and Leupeptin were from Sigma-Aldrich (Dorset, UK).

### Cell culture

HT1080 cells were obtained from Prof Chris Marshall (Institute of Cancer Research), A375P cells from Prof Richard Hynes (HHMI, MIT,

USA), SKMEL28 cells from Prof Richard Marais (Cancer Research UK Manchester Institute, Manchester, UK) and MDA-MB-231 cells were from Prof Clare Isacke (Institute of Cancer Research). 4599 (from Richard Marais) were established from the C57BL/6 mouse model Braf + /LSL-V600E;Tyr::CreERT2 + /o<sup>30</sup>.

For the spontaneous model of melanoma metastasis using 4599 were virally transduced to express NIS-mCherry as described in Maiques O in ref. 31. We used them for Fig. 3a–g.

Isolation of murine melanoma cells and ex vivo cultures were generated after intradermal injection using naïve 4599 (no

**Fig. 6 | Matrix organisation changes result in Rho-ROCK engagement and uncoupling of Myosin II from vinculin.** **a** Confocal SoRa images of HT1080 Fibrosarcoma cells showing nuclei (blue), F-actin (magenta), pMLC2 (cyan), and Vinculin (green) at increasing collagen concentrations (1.7–6.6 mg/ml). Scale bars: 10  $\mu$ m, insets 2  $\mu$ m. **b** Quantification of Vinculin/cell area (%) and percentage of pMLC2/Vinculin levels at the indicated collagen I concentrations. Left,  $n = 35, 28$  and  $28$  cells and right,  $n = 23, 25$  and  $22$  cells, three independent experiments. **c** Western blot analysis of Vinculin levels in HT1080 cells grown in different collagen I concentration gels.  $n = 3$  independent experiments. Vinculin and GAPDH were run in the same gel. **d** Confocal SoRa images of HT1080 Fibrosarcoma cells showing nuclei (blue), F-actin (magenta), pMLC2 (cyan), and Vinculin (green)  $\pm$  protease inhibitors (PI) at 4 h and 24 h. Scale bars: 10  $\mu$ m, insets 2  $\mu$ m. **e** Quantification of Vinculin/cell area (%) and percentage of pMLC2/Vinculin levels  $\pm$  PI. Left,  $n = 23, 18$  and  $21$  cells and right,  $n = 30, 27$  and  $25$  cells, three independent experiments. **f** Western blot

analysis of Vinculin levels  $\pm$ PI.  $n = 3$  independent experiments. Vinculin and GAPDH were run in the same gel. **g** RhoA and RhoC activation by pull-down assays in HT1080 cells  $\pm$ PI after 2 h treatment, with quantification of GTP-bound and total protein levels.  $n = 3$  independent experiments. **h** Immunofluorescence images showing F-actin and pMLC2 in HT1080 cells  $\pm$ PI and ROCK inhibitor (HI152) at 4 h. Scale bar: 20  $\mu$ m. **i** Quantification of cell rounding index and pMLC2/cell area from conditions in (h).  $n = 61, 66$  and  $59$  cells, three independent experiments. Unpaired  $t$ -test for pull-down assays (g) and One-way ANOVA with Tukey post-hoc test for all other comparisons (b left, c, e left, f, i). Two-way ANOVA with Tukey post-hoc (b right and e right). Data displayed as violin plots showing individual data points and medians (b left, e left, i), bar plot with mean and SD (b, right, c, e right, f, g). Cartoons in Fig. 6 (a, d, g, h) created in BioRender. Maiques, O. (2025) <https://BioRender.com/c83e894>.

plasmid) (Fig. 3h–k). (see animal methods for orthotopic injection). After 28 days from injection animals were sacrificed and primary tumours and lungs were removed transferred in falcon tubes with PBS  $-/-$   $\text{CaCl}_2/\text{MgCl}_2$  and kept in ice before subjecting to tumour cell isolation. Before cell isolation, primary tumours were processed as shown in diagram in Supplementary Table 1. Primary tumours were divided into two parts using a scalpel; one part was kept in 4% formaldehyde solution for paraffinization, while the second part was used for tumour cell isolation. For the latter, scissors and scalpel were used to collect the centre of the tumour or TB. For the IF, the peritumoral semi-transparent area with more fat tissue was collected, which contained the DIF area. The PIF was collected removing TB and DIF areas. To enrich populations, a pool of 6 primary tumours per area was used. For the lung where metastases were observed after postmortem examination, 3 lobules from each mouse were collected (total of 6 mice), the other remaining 2 lobules per mice were used for FFPE. Collected material for cell isolation was transferred to solutions with a mixture of Liberases (TH and TM, 75  $\mu$ g/ml each, Roche Diagnostics) and 1  $\mu$ g/ml DNase I (Sigma) in HBSS, digested briefly with gentle MACS Dissociator (Miltenyi Biotec) and transferred for 30 min at 37  $^\circ\text{C}$  shaking, and then passed through 100  $\mu$ m strainers. After digestion, cells were passed through the sorter ARIA Fusion (Becton Dickinson) using naïve 4599 as control. Cells were maintained in DMEM containing 10% foetal calf serum (FCS).

4599 TB, PIF, DIF and MET were isolated from naïve 4599 injected orthotopically into the skin of female 6–8 weeks old NXG (NOD-Prkdcscid-Il2rgtm1/Rj) mice (Janvier-Labs) at the experimental end point (28 days).

### Transfection and RNAi

For HT1080 cells, 200,000 cells were plated per 35 mm dish and transfected the next day with 20–40 nM SmartPool (SP) or individual OTs (On Targetplus) siRNA oligonucleotides, using Optimem-I and Lipofectamine 2000 (Invitrogen). Forty-eight hours after transfection cells were seeded on collagen in 10% FBS, allowed to attach overnight and treatments were added were indicated.

### siRNA sequences

All siRNA were from Dharmacon (Lafayette, USA). siRNA stocks were centrifuged, diluted in 1X siRNA resuspension buffer (Dharmacon) for a stock concentration of 100  $\mu$ M and allowed to mix via rotation at room temperature for 30 min. (Supplementary Table 3).

### Cell culture on thick layers of collagen I

Standard collagen unless differently stated, was fibrillar bovine dermal atelo Type-I Collagen solution (3 mg/ml) (#5005; PureCol, Advanced BioMatrix) and prepared at 1.7 mg/ml (Supplementary Table 4). For increasing collagen concentrations atelo Type-I Collagen solution (10 mg/ml) (#5133; FibrilCol, Advanced BioMatrix) was prepared at 1.7, 3.5 and 6.6 mg/ml (Supplementary Table 4). For radial alignment

experiment using Marangoni flows fibrillar bovine dermal telo Type-I Collagen solution (3 mg/ml) (#5026, TeloCol-3, Advanced BioMatrix) and prepared at 1.7 mg/ml (Supplementary Table 4).

PureCol and FibrilCol experiments were performed using the following volumes, 100  $\mu$ l per well in 96-well plates (immunofluorescence); 300  $\mu$ l per well in 24-well plates (cell morphology), 700  $\mu$ l per well in 12-well plates (immunoblotting). After collagen gel polymerization for 4 h, cells were seeded on top of collagen in medium containing 10% FCS, allowed to adhere for 24 h and then treatments were added in 1% FBS.

### Self-assembly of collagen fibres using Marangoni flows

To generate in vitro aligned collagen matrices, we used the protocol described in Nerger et al.<sup>36</sup>, with some minor modifications. In brief, T24 (Corning™ Costar™ 24-well Clear TC-treated) or T6 well plates (Corning™ Costar™ 6-well Clear TC-treated) were prepared drawing a circle with hydrophobic pen (ImmEdge® Hydrophobic Barrier PAP Pen (H-4000)) in the centre of the well, leaving space to add the saturated solution of  $\text{MgCl}_2$  around the well perimeter.

Simultaneously, type I bovine telo-collagen solution (Telocol) at 1.7 mg/ml was prepared to embed the cells as shown in Supplementary Table 4. Collagen concentration was adjusted using PBS, water and the pH of the resulting mixture was adjusted using the manufacturers' neutralizing solution (Advanced BioMatrix). Cell-laden hydrogels: cells were mixed with collagen final solution and plated according to the following instructions: for morphological assessment and immunofluorescence imaging either T12 or T24 well plates were used at a concentration of 100,000 cells/300  $\mu$ l well, and 12,000 cells/100  $\mu$ l well. For biochemistry and memory experiments, T6 were used a concentration of 300,000 cells/ 100  $\mu$ l well. For spheroids assays, the spheroid was collected and embedded in the centre before collagen had polymerized, using T12 plates.

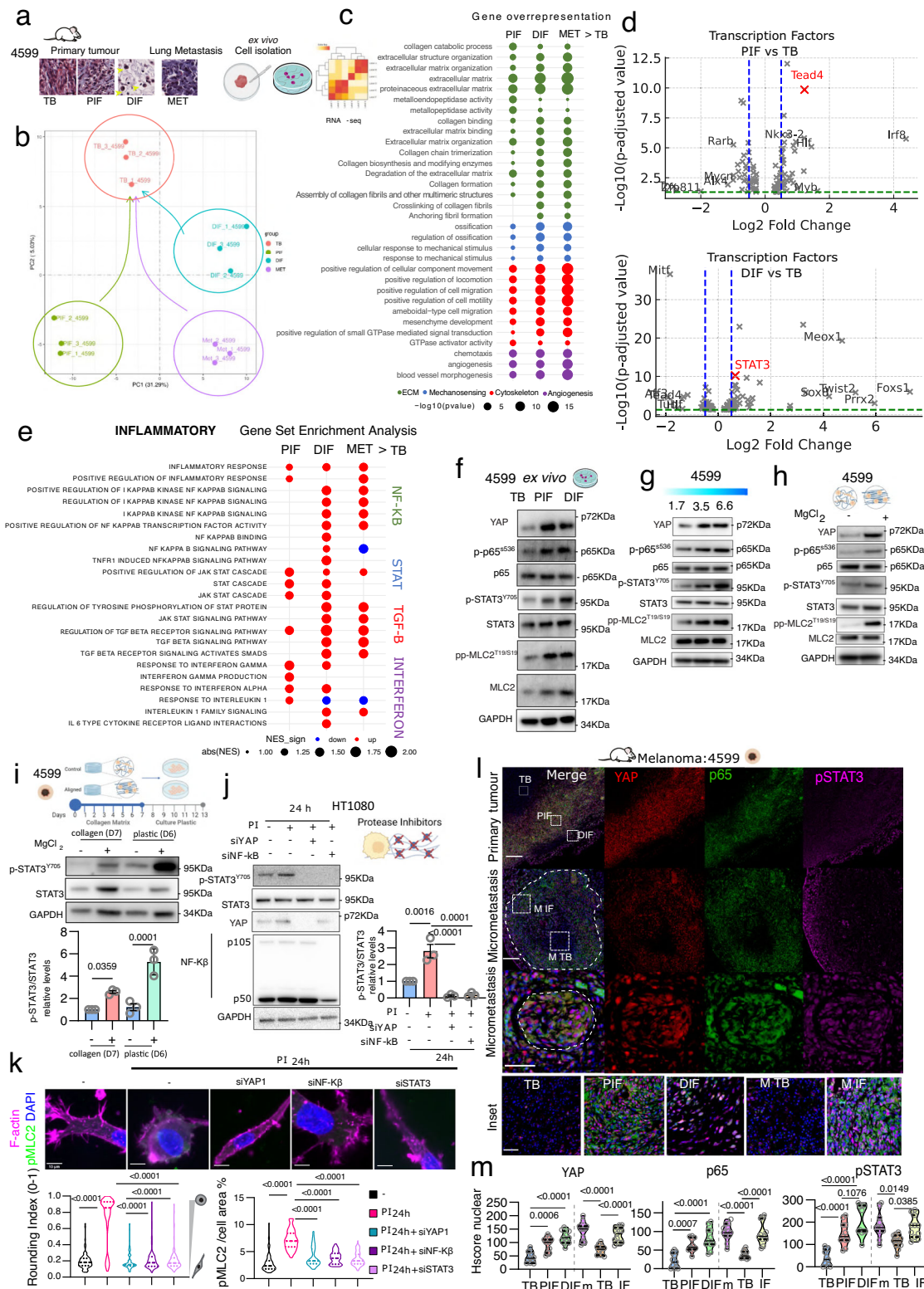
The collagen solution was placed inside the circle created with the PAP-Pen. After collagen polymerisation (40 min -1 h), salt ( $\text{MgCl}_2$ ) was carefully removed using PBS 1X avoiding salt touching collagen to finally fill the well with DMEM + 10% FBS.

For immunofluorescence imaging experiments, cells were left for 24 h in complete media and deprived to 1% FBS for 24 h before fixation and staining. For biochemistry experiments and establishment of mechanical memory, cells remained for 6 days in complete media (10% FBS) changed every 48 h and deprived to 1% FBS the 7th Day. Next, hydrogels were digested (see Collagen cell extraction section), and cells were pelleted down. For immunoblotting, cells were lysed with Laemli buffer followed by protein extraction. For mechanical memory experiments, cells were plated in T6 (plastic adherent) plates for expansion.

### Organotypics

Five hundred thousand HT1080 cells were plated on the top of 1 ml of matrix gel, which polymerized 1 h at 37  $^\circ\text{C}$  before adding the cells. The





next day, the gel was mounted on a metal bridge and fed from underneath with changes of 10% FCS media with treatment (vehicle or Plmix) every day. After 5 days, cultures were fixed (4% paraformaldehyde + 0.25% glutaraldehyde in PBS) embedded in paraffin blocks, sectioned, and stained with H&E. The type of invasion was calculated from ImageJ measurements.

**Cell extraction from collagen gels**

Collagen matrices were collected to a falcon tube with HBSS and Collagenase (Gibco). Gels were left at 37 °C during 30 mins on a shaker. Once the collagen was dissolved, the total volume was centrifuged in a falcon tube at 300 g for 5 mins. Cell pellets were resuspended in PBS 1X and cells counted for further downstream analysis.

**Fig. 7 | Matrix organisation drives a pro-metastatic transcriptional program.** **a** Mouse melanoma model showing intradermal injection of 4599 cells leading to lung metastasis. Cells isolated from different tumour areas (TB, PIF, DIF, Metastasis) for ex vivo experiments and RNA-seq. **b** Principal component analysis of 4599 cells' transcriptome from different tumour regions.  $n = 3$  independent experiments. **c** Gene overrepresentation analysis comparing PIF, DIF, and MET versus TB, grouped by ECM, Mechano-sensing, Cytoskeleton, and Angiogenesis signatures. **d** Volcano plots of transcription factors in PIF versus TB and DIF versus TB. Threshold:  $-0.5 < \text{Log}_2\text{FC} < 0.5$ ,  $-\text{Log}_{10}$  p-adjusted value. **e** GSEA analysis of inflammatory pathways, comparing PIF, DIF, and Met to TB. Dotplot shows normalized enrichment scores (FDR < 0.1). **f–h** Immunoblots showing YAP, p-p65, p65, p-STAT3, STAT3, pp-MLC2, and MLC2 protein levels in 4599 cells from different tumour areas ( $n = 5$  independent experiments), collagen concentrations ( $n = 4$ ), and aligned/non-aligned matrix ( $n = 3$ ). GAPDH is used as loading control. Quantification in Supplementary Fig. 7g. The samples for each panel derive from the same experiment but different gels for STAT3, MLC2 and GAPDH, another for p-STAT3<sup>Y705</sup>, pp-MLC2<sup>T19/S19</sup>, another for p65, another for p-p65<sup>S36</sup>, and another YAP were processed in parallel. **i** Top, diagram of experimental setting showing priming in  $\pm \text{MgCl}_2$  (7 days), and further culture in plastic (6 days). Bottom, corresponding p-STAT3/STAT3 protein levels in 4599 cells and quantification. GAPDH is used as

loading control.  $n = 3$  independent experiments. The samples derive from the same experiment but different gels for p-STAT3<sup>Y705</sup> and GAPDH, and another for STAT3 were processed in parallel. **j** Left, protein levels of p-STAT3/STAT3 in HT1080 cells after YAP or NF- $\kappa$ B knockdown with PI treatment (24 h). GAPDH is used as loading control. Corresponding quantification of p-STAT3/STAT3.  $n = 3$  independent experiments. The samples derive from the same experiment but different gels for p-STAT3<sup>Y705</sup> and GAPDH, another for STAT3, another for YAP1 and another for NF- $\kappa$ B1 were processed in parallel. **k** Top, confocal images showing F-actin, pMLC2, and nuclei after PI treatment with siYAP1, siNF- $\kappa$ B1, or siSTAT3. Bottom, corresponding cell rounding index and pMLC2/cell area quantification. Scale bar: 10  $\mu\text{m}$ .  $n = 91, 97, 91, 91$  and 92 cells, three independent experiments. **l** Multiplex immunohistochemistry of YAP (red), p65 (green), p-STAT3 (magenta) in 4599 primary tumours and lung metastases. Scale bars: 200  $\mu\text{m}$  (primary, macro), 50  $\mu\text{m}$  (micro, insets). **m** Nuclear H-score quantification (0–300) of transcription factors across tumour regions from (l).  $n = 11/\text{group}$ . One-way ANOVA with Šidák (l, j, k) and Tukey (m) post-hoc test. Data displayed as violin plots showing individual data points and medians (k, m), bar plot with mean and SD (l, j). Cartoons in Fig. 7 (a, f, h, i, j, l) created with BioRender.com. created with BioRender Maiques, O. (2025) <https://BioRender.com/z57v040> <https://BioRender.com/f02u038>.

### Immunoblotting

Cells were lysed in Laemmli sample buffer and sonicated for 15 s before centrifugation. Cell lysates were separated using precast 4–12% gradient SDS–polyacrylamide gel electrophoresis (SDS–PAGE) gels (Life Technologies) in non-reducing conditions and transferred subsequently to PVDF filters. ECL Plus or Prime ECL detection Systems (GE Healthcare) with HRP-conjugated secondary antibodies (GE Healthcare) were used for detection. Bands were quantified using ImageJ.

### RhoA/C-GTP pulldown assay

$2 \times 10^5$  cells/well were seeded on 6-well plates, treated with protease inhibitors for 2 h as indicated. Cells were lysed in buffer containing 50 mM Tris pH7.4, 10% glycerol, 1% NP40, 5 mM MgCl<sub>2</sub>, 100 mM NaCl, 1 mM DTT and EDTA free protease inhibitor and spun down. 10% of protein lysate was separated for determination of total RhoA and RhoC levels. The remaining protein lysate was incubated with Glutathione S-transferase (GST)-conjugated with Rhotekin RBD beads for 1 h. Beads were collected by centrifugation, washed, and resuspended in LDS loading buffer. All samples were boiled for 5 min and resolved by SDS-polyacrylamide gels electrophoresis. RhoA, RhoC, Tubulin and GAPDH proteins were detected via immunoblot.

### Gelatin zymography

HT1080 conditioned media was loaded on 10% SDS-polyacrylamide gels containing 0.3% gelatin (Sigma) in non-reduced protein sample. Following electrophoresis, proteins were renatured by incubating gels in 2.5% Triton X-100 for 2 h at 37 °C. Gels were then washed three times in distilled water and incubated in substrate buffer (50 mM Tris, pH 7.4, and 5 mM CaCl<sub>2</sub>) at 37 °C for 18 h with gentle shaking. Gels were stained with 0.1% Coomassie Blue R-250 (Sigma) and destained in 7% acetic acid. Enzymatic activities appear as cleared bands in a dark background.

### Immunofluorescence

Cells were seeded on collagen I in glass-bottomed dishes (MatTek, Ashland, MA, USA) and immunostained as described<sup>57</sup>. Cells were fixed (4% formaldehyde), permeabilized (0.2% Triton X-100; except for COL1- $\beta$ C immunostaining, in which cells were not permeabilized), blocked in 5% bovine serum albumin (BSA) and immunostained with specific antibodies diluted in 5% BSA, which were detected with secondary antibodies conjugated to either AlexaFluor488, -546, or -647 (Life Technologies). F-actin was stained using AlexaFluor546-

phalloidin (Life Technologies) or AlexaFluor647-phalloidin (Life Technologies).

### Confocal images were analysed using ImageJ

-For cell morphology, the shape descriptor 'roundness' in ImageJ was used after manually drawing around the cell shape using F-actin-staining images.

-Phospho-MLC2 fluorescence signal was quantified calculating the pixel intensity in single cells relative to the cell area.

-Percentage of nuclear YAP was calculated by measuring YAP fluorescence signal.

-Reflectance/matrix signal within 10  $\mu\text{m}$  from the edge of single cells was quantified in single cells and calculated relative to the cell perimeter.

-For measurement of collagen degradation, COL1- $\beta$ C fluorescence signal within 15  $\mu\text{m}$  from the edge of single cells was quantified and calculated relative to the cell perimeter<sup>57</sup>.

### Phase-contrast microscopy

Static phase contrast images were obtained on a OIQClick FM12 microscope camera attached to a Nikon TX-100 inverted phase-contrast microscope using a Nikon LW 10x objective. Images were acquired using QCapture Pro 7 Software.

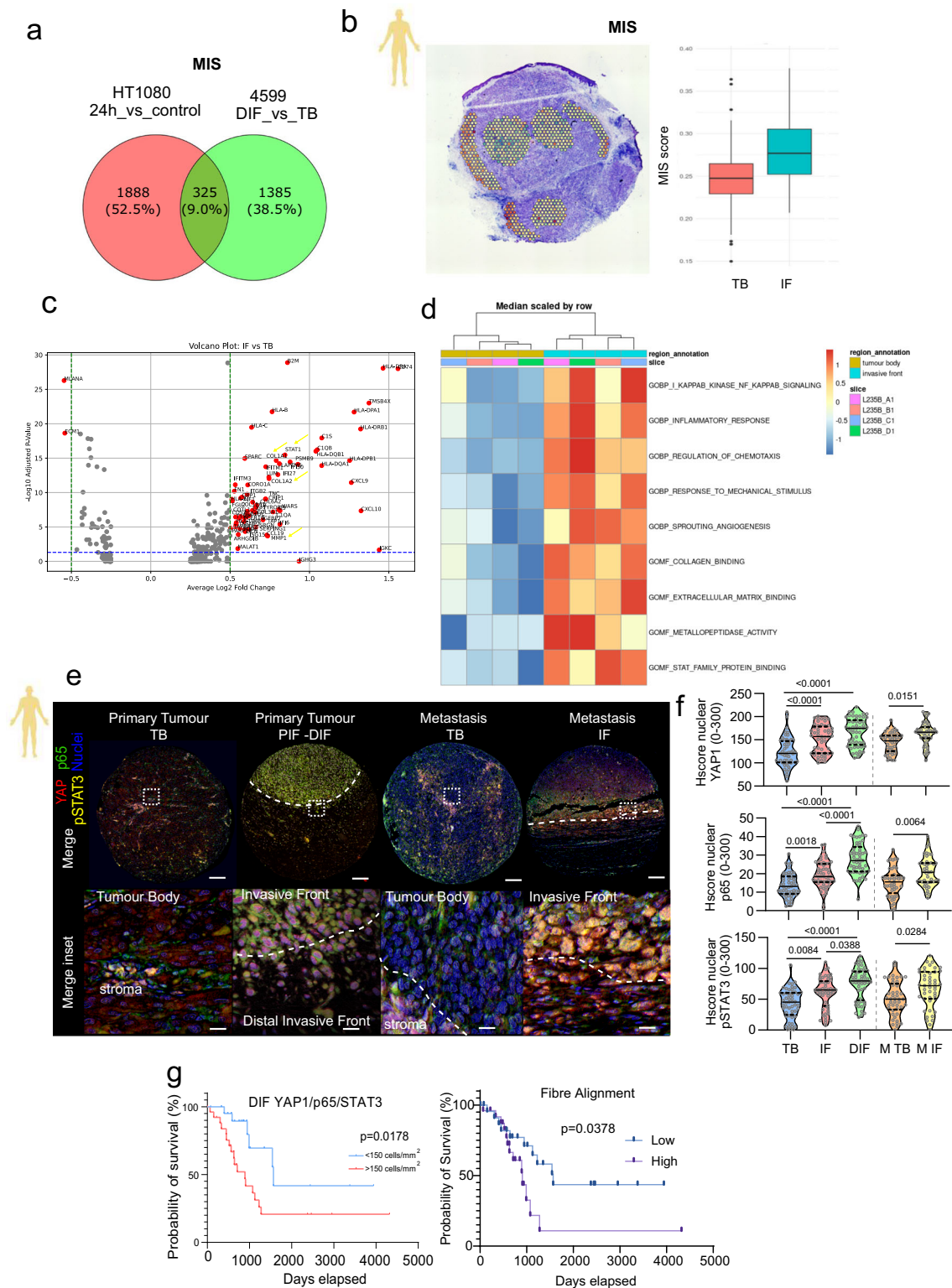
### Confocal microscopy

Confocal imaging was performed with Zeiss LSM 510, 710 and 880 with Airyscan Fast confocal microscope (Carl Zeiss) with C-Apochromat x 10/1.2, 40/1.2 (oil) and 63/1.2 (oil) objectives lenses and Zen software (Carl Zeiss). Reflectance imaging of the matrix was performed by collecting the backscattered light. Since reflectance is a surface property, extreme caution was taken to ensure the acquisition of images at the same height across all conditions.

Fixed samples were removed using forceps, turned over a MatTek dish so that the top surface of the collagen with the cells was in contact with the coverslip and then imaged using an inverted setup. Single confocal z-slices (1024×1024 pixels, 8-bit; 0.7x zoom) were taken across the mid-plane of the cells. For z-stacks used in analyses of collagen attachments, 30  $\mu\text{m}$  thick stacks were taken with a fixed step size of 0.5  $\mu\text{m}$  (512 × 512 pixels, 8-bit; 0.7x zoom).

### Multiphoton microscopy and second harmonic generation (SHG)

Imaging was performed using a SP8DIVE (Leica) upright multiphoton microscope and using 25x/1.0 W IR Apo with motCorr objective. The SHG was generated with an InSight® DS +™ a tunable 680–1300 nm IR



pulsed solid-state laser plus a 1045 nm fixed line (Spectra-Physics), using a laser pulsation at 900 nm with a band-pass filter spanning 10 to 20 nm at 450 nm, or using laser pulsation beam at 1300 nm with a relatively narrow band-pass filter at 650 nm. Samples were counter stained with Draq5 (1:2000, eBioscience) for nuclear staining, CK19 for BRCA tumours and Melanoma marker for Melanoma (see antibodies and inhibitors section).

### Super-resolution spinning disk microscopy

Vinculin and pMLC2 imaging was performed using Super Resolution Spinning Disk (TIRF/STORM/SoRa) with C-Apochromat X 63/1.2 oil objective lens, CSU-W1 camera and i3 Marianas software. z-stacks were used to analyse collagen attachment, 30  $\mu\text{m}$ -thick stacks were taken with a fixed step size of 0.5  $\mu\text{m}$  (51024 $\times$ 1024 pixels, 16-bit; 4x zoom).



**Fig. 8 | Matrix organization drives a pro-metastatic transcriptional program.** **a** Venn diagram showing Mechano-Inflammatory signature (MIS) derived from 4599 cells extracted from TB and DIF and from HT1080 treated with PI for 24 h. **b** Overlapping genes from (a) - conserved signature- were scored on the Visium array spots in a representative section of human melanoma lymph node metastasis. Annotations correspond to TB and IF areas.  $n = 4$  slices were analysed. Box plot shows the comparison between TB and IF annotations.  $n = 12$  TB annotations and  $n = 12$  IF annotations were analysed. **c** Volcano plot showing DEGs upon IF and TB comparison from spatial transcriptomics defined annotations. Highlighted in red DEGs that present average log2 fold change  $>0.5$  and  $-\log_{10}$  adjusted  $p$ -value. **d** Heatmap shows median scaled by row, displaying Gene Ontology Biological Pathways (GOBP) and Molecular Functions (GOMF) terms separated by regions (TB

and IF) and slices from Visium array analysed in melanoma metastasis samples. Z-score scale. **e** Representative merged multiplex images of primary and metastatic lesions of melanoma tumours. (bottom) Inset of merged multiplex. Nuclei were visualized with Haematoxylin stain (blue). Scale bar: 100  $\mu\text{m}$ . Scale bar insets: 20  $\mu\text{m}$ . **f** H-score quantification (0-300) of YAP1, p65 and pSTAT3 in the primary and metastatic lesions.  $n = 53$  primary and 45 metastatic lesions. **g** Kaplan-Meier curve showing overall survival with the quantification of amoeboid cells YAP1, p65 and pSTAT3 positive in the DIF area (left). Kaplan-Meier curve displays the overall survival comparing high and low fibre alignment (right). One-way ANOVA with Tukey post-hoc test (f). Data displayed as violin plots showing individual data points and medians (f). Cartoons in Fig. 8 (b, e) Created in BioRender. Maiques, O. (2024) <https://BioRender.com/h15l089>.

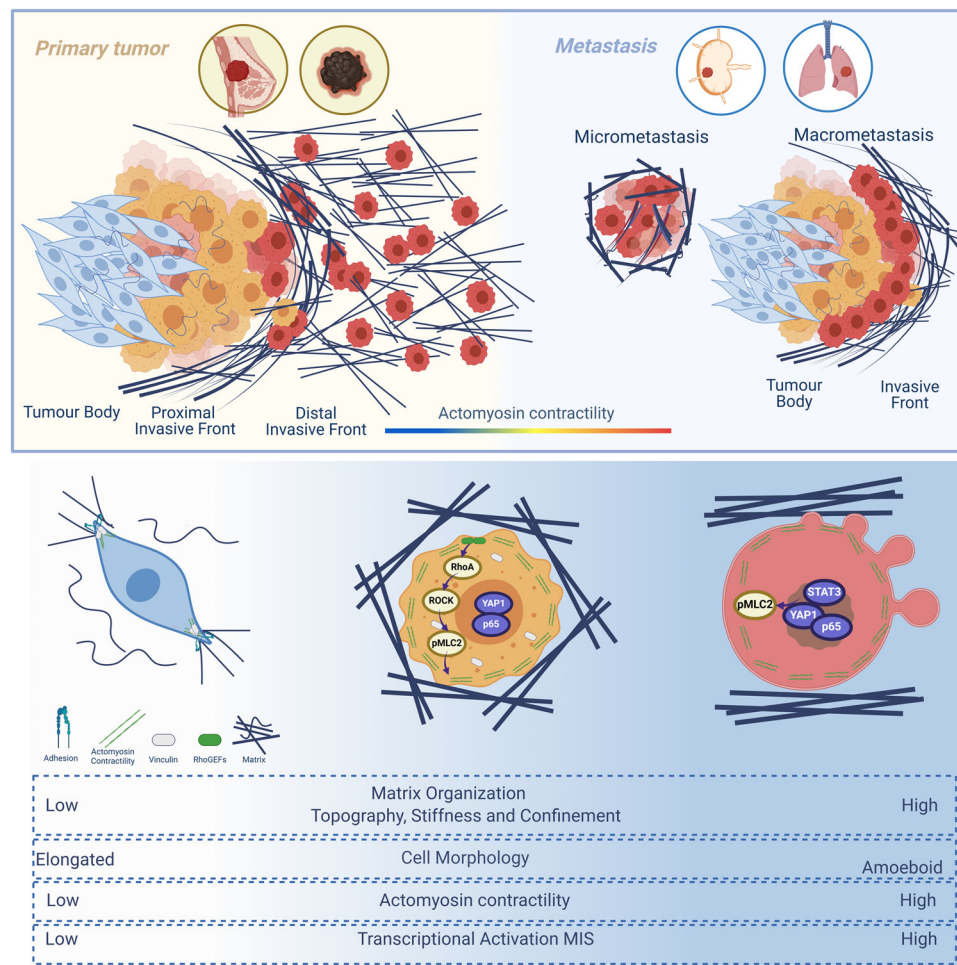


**Fig. 9 | Model.** Matrix organisation in primary tumours and metastasis: matrix heterogenous distribution in human solid tumours coupled to changes in the cytoskeleton and invasive patterns. The observations in primary tumour are mirrored in metastatic lesions. Mechanism at the cellular level (bottom): cancer cells under confinement, imposed by increased matrix, retract their protrusions and

contract their cytoskeleton reducing cell-matrix adhesion. This retraction is accompanied by vinculin uncoupling from adhesions and activation of RhoA-ROCK-Myosin II axis leading to long-term transcriptional reprogramming orchestrated by YAP1-NF- $\kappa$ B and STAT3. Figure created in BioRender. Maiques, O. (2025) <https://BioRender.com/v18d918>.

### Atomic force microscopy

The mechanical properties of collagen I gels were measured in gels exposed to H<sub>2</sub>O (control,  $n = 5$ ) or MgCl<sub>2</sub> ( $n = 5$ ) using a JPK NanoWizard AFM (Bruker). For each gel, 100 points from three different areas were measured using a MLCT-O10-E cantilever (Bruker) manually conjugated to a polystyrene bead of 7.3  $\mu\text{m}$  in radius (F21010, Invitrogen) using UV curing adhesive (267423, Rapid Electronics Ltd). The spring constant was 0.054 N/m. Young's elastic modulus of each gel was estimated using the Hertz model, with a 0.5 Poisson's ratio, using the JPK Data Processing software (v8.0.92, Bruker).

### Sphere invasion assay

For sphere preparation, 4599 TB and 4599 DIF or 4599 MET labelled cells using cellTracker dyes (see vital dye cell staining) were mixed to a 1:1 ratio to a final cell number of 80,000 cells in 20% methylcellulose and 80% DMEM + 10% FBS in total volume of 1 ml. 25  $\mu\text{l}$  drops were deposited in the lid of a round petri dish, carefully inverting the lid to natural position and adding PBS in the base. For experiments using HT1080 cells, spheres were made at 40,000 total number of cells per 1 ml of total volume. The spheres were formed in hanging drops for 24 h. After that, spheres were embedded in PureCol 1.7 mg/ml (Advanced BioMatrix). For alignment

experiments, cells were embedded in TeloCol 1.7 mg/ml. The spheroids were fixed in 4% paraformaldehyde (PFA) after 24 h or 72 h.

Brightfield images of spheroids embedded in a collagen matrix were taken at end point. An annotation of the core of the spheroid was created and was then expanded every 300  $\mu\text{m}$ . A pixel classifier was created to differentiate spheroid from background/matrix. Random trees classifier was used for training while resolution of the mask was set as “High resolution”, and Features were selected scale 1.0, 2.0 and Gaussian, Hessian determinant, Hessian max eigenvalue, Hessian middle eigenvalue and Hessian min eigenvalue. Mask detecting spheroid was created as annotation.

### 3D invasion

For 3D invasion assay, cells were extracted from non-aligned (H2O) and aligned ( $\text{MgCl}_2$ ) matrices and labelled with different colour dyes (see Colour coding vital dye cell staining). 15 K cells were resuspended in Bovine dermal fibrillar collagen (PureCol, Cat. 5005 Advanced Bio-Matrix) plated in a 96-well plate and spun down before matrix polymerisation. After the matrix was polymerised, 10% FBS-containing media was added on top of the matrix as chemoattractant. After 24 h, cells were fixed and imaged using a Zeiss LSM 710 confocal microscope. Invasion was calculated as number of invading cells at 50  $\mu\text{m}$  divided by the number of cells at the bottom.

### Vital dye cell staining

For vital dye staining, cells were suspended in 10  $\mu\text{M}$  CMFDA-Green (C7025, Life Technologies) or 10  $\mu\text{M}$  CMRA-Orange (C34551, Life Technologies) in 1 ml OPTIMEM (31985070, Gibco). Cells were stained for 15 min at 37 °C and washed twice with PBS 1X. Cells were suspended in 1 ml PBS 1X and counted to use them at 1:1 ratio for further experiments.

### Animal experiments

**Intradermal tumours.** All animals were maintained under specific pathogen-free conditions and handled in accordance with the Institutional Committees on Animal Welfare of the UK Home Office (The Home Office Animals Scientific Procedures Act, 1986). All animal experiments were approved by the Ethical Review Process Committees at Barts Cancer Institute and King's College London, and carried out under licences from the Home Office, UK. 6–12 weeks old male (Figs. 3a–f, 7l, m) and female (Figs. 3h–k, 7a–f) mice were used. Animals were housed in groups of 4–5 mice per cage with access to food and water ad libitum. Mice were maintained on an alternating 12 h light-dark cycle, with controlled room temperature ( $21 \pm 1$  °C) and relative humidity (40–60 %). The maximal tumour size permitted in the animal license is 1.5 cm<sup>3</sup> for a single tumour. 200,000 4599 mouse melanoma cells in 30  $\mu\text{L}$  PBS were injected intradermally into NOD. Cg-Prkdc<sup>scid</sup> Il2rg<sup>tm1Wjl</sup>/SzJ mice (NSG; purchased from Charles River UK). Tumours were allowed to grow during 30 days after intradermal injection<sup>31</sup> and primary tumours and Lungs with apparent presence of macro-metastasis were collected. Tissues were fixed in 4% formaldehyde for 24 h at 4 °C, following this, tissues were transferred to histology cassettes and dehydrated for 1 h in 70% ethanol, 2 h in 96% ethanol, 2 h in 100% ethanol and 1.5 h in xylene. Following dehydration, samples were transferred to a paraffin bath set to 60 °C for 1.5 h. Samples were then embedded using an embedding machine and allowed to solidify on a cold plate. Embedded samples were kept at 4 °C prior to sectioning.

**Lung colonisation assay.** 4599, 4599 TB and 4599 DIF murine melanoma cells were used. 4599 TB were mixed with 4599 DIF with different dyes (see Colour coding vital dye cell staining). 4599 naïve cells were primed for 7 days with TeloCol (1.7 mg/ml) non-aligned (H<sub>2</sub>O) and aligned ( $\text{MgCl}_2$ ) collagen matrices.

Cells were labelled with different vital dyes following above protocol. Priming experiments required extracting cells from collagen

using collagenase (see collagenase section) and expanded on plastic for 6 days. Equal numbers of CMFDA-Green and CMRA-Orange labelled cells were mixed (500,000 cells of each type), resuspended in 0.2 ml PBS 1x and injected into tail vein of 9–10-week-old female NOD/SCID/ IL2R $\gamma$ <sup>-/-</sup> mice (NSG, Charles River). Experiments were repeated inverting the colours to ensure reproducibility regardless of the vital dye used.

Mice were sacrificed after 30 min (to confirm equal cell numbers had been injected and reached the lung) and 48 h after tail vein injection to assess lung colonisation. Lungs were extracted, washed with PBS 1X (with calcium/magnesium) twice and fixed with 4% formaldehyde for 16 h at 4 °C and counterstained with DAPI (1:2000 dilution). Lungs were examined under a Zeiss LSM 880 confocal microscope (Carl Zeiss) with a 20X objective and imaging 2 × 2 tiles. Data are presented as percentage of field of area covered by fluorescence, and 15 fields per mouse were analysed.  $n = 7$  mice/condition for each experiment (2 mice sacrificed after 30 min and 5 mice 48 h after tail vein injection),  $n = 2$  independent experiments.

QuPath was used for image analysis of the lung tissues. An average threshold from three channels (Blue, Green and Orange) was created and then used as a general mask and as a single annotation. Two independent thresholds were created for green and Orange using simple threshold tool. Threshold masks for Green and Orange were created as detection measurements inside the higher-level annotation.

### Histopathology

**Human case selection.** We used formalin-fixed paraffin-embedded (FFPE) of human primary melanomas (53 patients), and metastasis (45 patients); breast cancer (BRCA) samples (30 patients) obtained from Hospital Arnau de Vilanova, Lleida and Hospital de Bellvitge, Barcelona (Spain) (See supplementary Data 1–3). Tumours were classified following the most recent World Health Organization criteria. The study was approved by the Ethical Committees of both Hospitals, and a specific informed consent was used. A tissue arrayer device (Beecher Instruments, Silver Spring, MD, U.S.A.) was used to construct the tissue microarrays (TMA). Two selected cylinders (1 mm in diameter for Melanoma; 0.4 mm for BRCA) from two different areas targeting TB and IF which contain PIF and DIF were included in each case.

**Tissue staining.** For Masson trichrome staining, samples were rehydrated, stained with Weigert's iron hematoxylin working solution for 10 min, stained in Biebrich scarlet-acid fuchsin solution for 10–15 min, differentiated in phosphomolybdic-phosphotungstic acid solution for 10–15 min, transferred to directly (without rinse) aniline blue solution and stained for 5–10 min. Finally, samples were rinsed briefly in distilled water and treated with 1% acetic acid solution for 2–5 min. Gomori staining was performed at Hospital Arnau de Vilanova, Lleida according to the manufacturers' instructions.

For immunohistochemistry, TMA blocks were sectioned (3  $\mu\text{m}$ -thick) and dried for 1 h at 65 °C before deparaffinization and rehydration. Antigen retrieval was performed in Antigen Unmasking Solution pH 6 (H-3300, Vector Labs) using a pressure cooker system (110 °C for 10 min). Samples were washed in Dako Wash Buffer (S3006). Primary antibody incubation was performed overnight at 4 °C with the antibodies listed below and concentration as explained in the antibodies and inhibitors section. Primary antibodies were diluted in Antibody Diluent Reagent Solution (003218, Invitrogen/ThermoFisher Scientific). Samples were washed and incubated with ImmPRESS® polymer secondary goat anti-rabbit antibody (goat anti-rabbit, RTU, Vector Labs, MP-7451) for 45 min. The reaction was developed using VIP peroxidase substrate solution (Vector Labs, SK-4600) for 10 min. All incubations were carried out at room temperature. Slides were counterstained with haematoxylin and mounted using DPX mounting medium (06522-500 ML, sigma). Slides were imaged using the Nano-Zoomer S210 slide scanner (Hamamatsu, Japan). Multiplex IHC was

used to assess amoeboid features, while staining and re-probing cycles were performed for Melanoma marker or CK-19, pMLC2 and total MLC2. Staining and re-probing cycles were also performed for YAP1, p65 and pSTAT3 staining (adapted from Maiques O<sup>32</sup>).

### Digital pathology

**Matrix analysis.** Masson's trichrome staining: FFPE tissue slides were processed following the pipeline in Supplementary Table 2. A ROI per zone in either TB, PIF or DIF was selected and created in QuPath<sup>24</sup>. Annotated regions were exported using a custom-made script. ROIs for BRCA were 482×482 pixels and for Melanoma 954×954 pixels (4.5251px/μm, both).

To analyse global matrix changes, we created a specific project in QuPath. Regions of Interest (ROIs) were loaded, and images were duplicated and categorized under Brightfield (other). Color deconvolution was performed using user-defined values. For Masson's Trichrome:

*Colour\_1: [r1]=0.43 [g1]=0.745 [b1]=0.51; Colour\_2: [r2]=0.758 [g2]=0.601 [b2]=0.255; Colour\_3: [r3]=0.501 [g3]=0.571 [b3]=0.65. For Gomori's Trichrome Colour\_1: [r1]=0.517 [g1]=0.682 [b1]=0.518; Colour\_2: [r2]=0.688 [g2]=0.577 [b2]=0.439; Colour\_3: [r3]=0.443 [g3]=0.583 [b3]=0.681.*

The first batch was used to calculate the percentage of matrix and matrix intensity. Fully annotated images were created, and the 'positive pixel count' plugin was executed as follows:

```
runPlugin('qupath.imagej.detect.tissue.PositivePixelCounterIJ',
'{"downsampleFactor":1,"gaussianSigmaMicrons":2.0,"thresholdStain1":0.2,"thresholdStain2":0.1,"addSummaryMeasurements":true,"clearParentMeasurements":true,"appendDetectionParameters":false,"legacyMeasurements0.1.2":false}').
```

Annotations were exported from all cases and Positive % of total ROI area was calculated. Detections were exported from all cases and DAB OD mean value was used as a proxy of stain 2 intensity or matrix values after colour deconvolution was applied.

The second batch of duplicated ROIs used the same colour deconvolution parameters. Subsequently, superpixel segmentation was performed using the Difference of Gaussian (DoG) method as follows:

```
runPlugin('qupath.imagej.superpixels.DoGSuperpixelsPlugin',
'{"downsampleFactor":1.0,"sigmaPixels":2.0,"minThreshold":10.0,"maxThreshold":200.0,"noiseThreshold":1.0}').
```

Afterwards, intensity values and Haralick features were added to the segmented masks as follows:

```
runPlugin('qupath.lib.algorithms.IntensityFeaturesPlugin',
'{"downsample":1.0,"region":"ROI","tileSizePixels":200.0,"colorOD":false,"colorStain1":false,"colorStain2":true,"colorStain3":false,"colorRed":false,"colorGreen":false,"colorBlue":false,"colorHue":false,"colorSaturation":false,"colorBrightness":false,"doMean":true,"doStdDev":false,"doMinMax":false,"doMedian":false,"doHaralick":true,"haralickDistance":1,"haralickBins":32}').
```

Haralick entropy, calculated from the gray-level co-occurrence matrix (GLCM), was used to assess the complexity of collagen matrix texture, with higher entropy values indicating greater alignment and organization of collagen fibres.

Detection measurements from each ROIs (TB, PIF, and DIF) were exported. A custom-made script in Python calculated the average of "ROI: 1.00 px per pixel: DAB: Haralick Entropy (F8)" per region. The script was developed using Python v3.8.2 and the Pandas library.

### Matrix topography

For trichrome staining, Channel 2 was extracted using color deconvolution parameters as outlined in the previous section, applying either Masson's or Gomori's trichrome values, as appropriate. Colour\_2 (matrix channel) was selected and converted to 8-bit, Enhanced Contrast and saturated 0.35 and set min:68 and max:255 for all ROIs using

Fiji-ImageJ in a custom script for all ROIs. For confocal images, reflectance channels were used without any pre-processing step.

Matrix topographical features such as Length, Width, Straightness and Angle orientation were calculated in CT-FIRE V5 stand-alone plugin Matlab following the author's instructions<sup>26,29</sup>. Minimum fibre length was amended to 10pxl, fibre line width to 0.2. A custom-made script using python 3.8.2 and pandas' library calculated the median of fibre length, width, straightness for each ROI analysed using the files' created and named as HistLEN', 'HistWID', 'HistSTR'. Pixel values were corrected to micron scale, obtained from the original image. For angle orientation: histograms from 0–180 angles were generated comparing PIF and DIF showing the percentage and SEM per bin. For matrix alignment, distance between fibres was calculated using CurveAlign. Alignment values were normalized to number of fibres per ROI and an Alignment score was calculated. For distance between fibres, the median per ROI was calculated using a custom-made script using python 3.8.2 and pandas' library. Median distance between fibres was normalized to microns using the scale factor from the original images. For fibre density, pixels<sup>2</sup> per ROI and scale factor were considered and represented in fibres per mm<sup>2</sup>. Overlay maps of fibre alignment were created using standard parameters but changing the "Heatmap Gaussian disc filter sigma (in pixels)" from 4 to 12.

**Gap analysis.** Confocal reflectance images were processed following MATLAB script provided <https://www.actonlab.co.uk/gap-analysis-matlab/> and used previously<sup>66</sup>.

**Multiplex IHC scoring.** TMAs were stained, stripped and reprobated consecutively within the same slide for pMLC2, total MLC2 and tumour markers. In case of melanoma, a pan-Melanoma marker was used, for BRCA TMA CK19 was used as a tumour marker. Using Multiview tool in QuPath, the TMAs of the three consecutive sections were displayed and ROIs were created. Using a custom-made script following the adapted protocol of staining, quantification was performed using QuPath 0.4.4<sup>24</sup> using Virtual multiplex pipeline adapted from Maiques O et al.<sup>32</sup>.

In summary, ROIs with overlapping regions from the same tissue with the three different markers (panMelanoma or CK19, pMLC2 and MLC2) were transferred to Fiji-ImageJ. Colour Deconvolution using H AEC channels was performed for each channel. VIP colour channels for three markers and nuclear markers were merged using a Stack. Using rigid registration, the images were aligned, and next pseudo-colour was applied and LUTs were inverted. The stack image was saved in TIFF and loaded in QuPath. Simple threshold for the cancer marker (pan-Melanoma or CK19) was created. Pixels were created as annotation masks and StarDist segmentation was applied<sup>67</sup>. Next, Intensity thresholds were selected for pMLC2 and MLC2. Detection measurements were exported and means per core were calculated for circularity, and H-score for pMLC2 and MLC2. Same pipeline was applied for mCherry, pMLC2 and MLC2. YAP, p65 and pSTAT3 analysis was done similarly measuring nuclear intensity.

### Microarray analysis

HT1080 cells treated with protease inhibitors for 4 and 24 h seeded on top of collagen I and RNA was extracted using Trizol (Invitrogen, Carlsbad, CA) followed by Qiagen RNeasy Midi Kit. cRNA was prepared according to the GeneChip Expression Analysis Technical Manual (Affymetrix), hybridized onto HU133A chips (Affymetrix), and scanned by a GeneArray@ 2500 Scanner (Affymetrix). Each sample was run in triplicate. Microarray data analysis was performed using R (version 2.9.2) (<http://www.R-project.org>) and Bioconductor version (2.4)<sup>68</sup>. Signal data were normalised using the robust multichip average (RMA) algorithm from the "Affy"<sup>69</sup> package with default parameters.

Network and enrichment analysis of the gene lists was performed using Ingenuity pathway analysis (IPA, Qiagen) and Cytoscape using



ClueGo module<sup>70</sup>. All IPA analysis was carried out with a threshold of  $p$ -value  $< 0.05$ . The comparisons were carried out between HT1080 control vs 4 h of protease inhibitor, HT1080 control vs 24 h of protease inhibitor. Hierarchical clustering was performed using Gennepattern<sup>71</sup>.

### RNAseq

4599 murine melanoma cells isolated from different tumour parts (TB, PIF, DIF and MET) were seeded on Fibrillar bovine dermal collagen 1.7 mg/ml (PureCol, Cat. 5005 Advanced BioMatrix) for 24 h DMEM + 10% FBS. Media was changed to DMEM + 1% FBS during 24 h before the RNA extraction. RNA was extracted using TRIzol (Invitrogen, Carlsbad, CA) followed by QIAGEN RNeasy Midi Kit. RNA integrity and quality was evaluated using RNA Qubit™ assay. Sequencing was performed using 150 bp paired end sequencing strategy using Illumina sequencing platform and PE150 Technology. The data output was 6 Gb.

Data quality control and filtering was performed using Fastq Software. Reads were mapped to *mus musculus* (GRCm38 – mm10) reference genome using Hisat2 v2.0.5 as mapping tool. Feature Counts v1.5.0-p3 function from HTseq software was used to count the reads numbers mapped to each gene. Fragments Per Kilobase of transcript sequence per Millions base pairs sequenced (FPKM) of each gene were calculated based on the length of the gene and reads count mapped to this gene.

DESeq2 R package (1.20.0) was used to obtain differential expression analysis. The resulting  $p$ -values were adjusted using the Benjamini and Hochberg's approach for controlling the false discovery rate. Genes with an adjusted  $p$ -value  $\leq 0.05$  found by DESeq2 were assigned as differentially expressed. The DEGs were further used for GO enrichment analysis implemented by the ClusterProfiler R package, in which gene length bias was corrected. GO terms with corrected  $p$ -value less than 0.05 were considered significantly enriched by DEGs. Gene overrepresentation, KEGG and Reactome pathway investigation was also performed using ClusterProfiler software and GSEA R package to provide the gene set enrichment analysis. The lists of gene signatures used are related to ECM, angiogenesis, mechano-sensing, cytoskeleton and inflammation.

The list of DEGs are from Novogene. List of DEGs was filtered to only include genes which are  $FDR \leq 0.05$ . The mouse genes were converted to human orthologous genes using mouse/human ortholog with phenotype mapping (<https://www.informatics.jax.org/downloads/reports/index.html>). Orthologous pairs from the HMD\_HumanPhenotype.rpt (accessed 16-Jun-2023) were used. R package ggvenn (0.1.10) was used to create the Venn diagram. The common gene signature list ( $n = 325$ ) is available in Supplementary Data 4.

### Spatial transcriptomics

Optimal Cutting Temperature compound (OCT) frozen tumour samples ( $n = 4$ ) were obtained from Cresciolli et al.<sup>72</sup>. Patient information included in ref. 72. Corresponding H&E from spatial transcriptomics analysis was used for Digital pathology analysis. Tissue scans were loaded in QuPath and cell detection plus machine-learning classification for Tumour, Stroma and Immune cells was performed. Visium 10x spatial transcriptomics of a melanoma tumour was used, showing the H&E staining, cell annotation and region of interest selection using QuPath. QuPath information was subsequently projected onto Visium spots.

Processed Visium samples from non-consecutive tumour slices were obtained upon request from Cresciolli et al.<sup>72</sup> as Seurat objects. FASTQ files were aligned to human reference genome (GRCh38-2020-A) using SpaceRanger v1.3.1 with default parameters. Seurat package version 4.3.0.1 was used with default parameters to create Seurat object<sup>73</sup>. Regions of interest (tumour body, invasive front) were manually annotated in QuPath and merged with Seurat objects.

The list of common genes ( $n = 325$ ) as obtained in section (xyz) was used to calculate the enrichment score per spot using the AddModuleScore function of Seurat with default parameters. This was

subsequently projected onto the tissue and summarized as boxplots. Additional enrichment scores were calculated for selected gene ontology pathways, using gene overrepresentation pathway definition version c5.all.v2023.1.Hs.symbols.gmt obtained from [www.gsea-msigdb.org](http://www.gsea-msigdb.org).

### MIS signature in patients

Clinical and transcriptomic data in relative z-scores were downloaded from cBioportal (<https://www.cbioportal.org/>) from 32 different TCGA projects included in the TCGA PanCancer Atlas Studies collection<sup>74</sup> and breast cancer patients from the METABRIC collection<sup>75</sup>. Patients were given a unique value for the gene signature calculated using the mean value of the individual z-scores of the genes included in the signature and separated between “high” and “low” signature using the median value of the signature expression. Kaplan-Meier survival curves and log-rank statistical values were obtained in R by using the package “Survival” and calculated for each TCGA project independently.

### Statistics & reproducibility

Statistical analysis was carried out on 3 or more independent experiments, using Graphpad Prism 9 and 10 (GraphPad Software, San Diego California USA, [www.graphpad.com](http://www.graphpad.com)). For western blots and data sets exhibiting normal distribution, two-tailed Student's t-test was performed to compare two sets of data, while ANOVA (Analysis of Variance) with Tukey's post-hoc test was carried out to compare 3 or more independent sets of data. In case of larger data sets exhibiting a non-normal distribution, non-parametric tests were used. A Mann-Whitney test was performed to compare two sets of data, while a non-parametric ANOVA with Kruskal–Wallis multiple comparisons test was carried out to compare 3 or more independent sets of data. The degree of statistical dependence of two variables was determined by Spearman's correlation test and Pearson's  $p$ -value calculated using GraphPad Prism. The threshold for statistical significance was set to a  $P$  value of less than 0.05. No statistical methods were used to calculate sample size. The investigators were not blinded to allocation during experiments and outcome assessment. The results of the experiments provided quantitative data that was analysed with the appropriate statistical tests to evaluate differences and statistical significance. Immunohistochemical analyses were blinded to clinical patient information.

### Reporting summary

Further information on research design is available in the Nature Portfolio Reporting Summary linked to this article.

### Data availability

RNAseq data and Microarray information have been deposited in the National Center for Biotechnology Information Gene Expression Omnibus. HT1080 microarray was deposited in Gene Expression Omnibus repository with reference number [GSE197310](https://www.ncbi.nlm.nih.gov/geo/query/acc.cgi?acc=GSE197310). 4599 ex vivo TB, PIF, DIF and MET RNAseq was deposited in Gene Expression Omnibus repository with reference number [GSE263097](https://www.ncbi.nlm.nih.gov/geo/query/acc.cgi?acc=GSE263097). All study data are included in the article and supporting information. Source data are provided as a Source Data file. Codes for image processing, data curation and plotting have been deposited in github [https://github.com/mAlqPath/ECM\\_Transcription](https://github.com/mAlqPath/ECM_Transcription). Source data are provided with this paper.

### References

- Winkler, J., Abisoye-Ogunniyan, A., Metcalf, K. J. & Werb, Z. Concepts of extracellular matrix remodelling in tumour progression and metastasis. *Nat. Commun.* **11**, 5120 (2020).
- Frantz, C., Stewart, K. M. & Weaver, V. M. *The Extracellular Matrix at a Glance*. *J. Cell Sci.* **123**, 4195–4200 (Company of Biologists, 2010).

3. Eble, J. A. & Niland, S. The extracellular matrix in tumor progression and metastasis. *Clin. Exp. Metastasis* **36**, 171–198 (2019).
4. Kaur, A. et al. Remodeling of the Collagen Matrix in Aging Skin Promotes Melanoma Metastasis and Affects Immune Cell Motility. *Cancer Discov.* **9**, 64–81 (2019).
5. Ecker, B. L. et al. Age-Related Changes in HAPLN1 Increase Lymphatic Permeability and Affect Routes of Melanoma Metastasis. *Cancer Discov.* **9**, 82–95 (2019).
6. Piersma, B., Hayward, M. K. & Weaver, V. M. Fibrosis and cancer: A strained relationship. *Biochim. Biophys. Acta Rev. Cancer* **1873**, 188356 (2020).
7. Pickup, M. W., Mouw, J. K. & Weaver, V. M. The extracellular matrix modulates the hallmarks of cancer. *EMBO Rep.* **15**, 1243–1253 (2014).
8. Provenzano, P. P. et al. Collagen reorganization at the tumor-stromal interface facilitates local invasion. *BMC Med.* **4**, 38 (2006).
9. Provenzano, P. P. et al. Nonlinear optical imaging of cellular processes in breast cancer. *Microsc. Microanal.* **14**, 532–548 (2008).
10. Conklin, M. W. et al. Aligned collagen is a prognostic signature for survival in human breast carcinoma. *Am. J. Pathol.* **178**, 1221–1232 (2011).
11. Provenzano, P. P., Inman, D. R., Eliceiri, K. W., Trier, S. M. & Keely, P. J. Contact guidance mediated three-dimensional cell migration is regulated by Rho/ROCK-dependent matrix reorganization. *Biophys. J.* **95**, 5374–5384 (2008).
12. Ray, A. et al. Anisotropic forces from spatially constrained focal adhesions mediate contact guidance directed cell migration. *Nat. Commun.* **8**, 1–17 (2017).
13. Park, D. et al. Extracellular matrix anisotropy is determined by TFAP2C-dependent regulation of cell collisions. *Nat. Mater.* **19**, 227–238 (2020).
14. Acerbi, I. et al. Human breast cancer invasion and aggression correlates with ECM stiffening and immune cell infiltration. *Integrative. Biol. (U. Kingd.)* **7**, 1120–1134 (2015).
15. Charras, G. & Sahai, E. Physical influences of the extracellular environment on cell migration. *Nat. Rev. Mol. Cell Biol.* **15**, 813–824 (2014).
16. Liu, Y. J. et al. Confinement and low adhesion induce fast amoeboid migration of slow mesenchymal cells. *Cell* **160**, 659–672 (2015).
17. Sanz-Moreno, V. et al. ROCK and JAK1 Signaling Cooperate to Control Actomyosin Contractility in Tumor Cells and Stroma. *Cancer Cell* **20**, 229–245 (2011).
18. Cantelli, G. et al. TGF-beta-Induced Transcription Sustains Amoeboid Melanoma Migration and Dissemination. *Curr. Biol.* **25**, 2899–2914 (2015).
19. Rodriguez-Hernandez, I. et al. WNT11-FZD7-DAAM1 signalling supports tumour initiating abilities and melanoma amoeboid invasion. *Nat. Commun.* **11**, 5315 (2020).
20. Laser-Azogui, A., Diamant-Levi, T., Israeli, S., Roytman, Y. & Tsarfaty, I. Met-induced membrane blebbing leads to amoeboid cell motility and invasion. *Oncogene* **33**, 1788–1798 (2014).
21. Odenthal, J., Takes, R. & Friedl, P. Plasticity of tumor cell invasion: governance by growth factors and cytokines. *Carcinogenesis* **37**, 1117–1128 (2016).
22. Ruprecht, V. et al. Cortical contractility triggers a stochastic switch to fast amoeboid cell motility. *Cell* **160**, 673–685 (2015).
23. Logue, J. S. et al. Erk regulation of actin capping and bundling by Eps8 promotes cortex tension and leader bleb-based migration. *Elife* **4**, e08314 (2015).
24. Bankhead, P. et al. QuPath: Open source software for digital pathology image analysis. *Sci. Rep.* **7**, 1–7 (2017).
25. Bredfeldt, J. S. et al. Automated quantification of aligned collagen for human breast carcinoma prognosis. *J. Pathol. Inf.* **5**, 28 (2014).
26. Bredfeldt, J. S. et al. Computational segmentation of collagen fibers from second-harmonic generation images of breast cancer. *J. Biomed. Opt.* **19**, 16007 (2014).
27. Chen, X., Nadiarynkh, O., Plotnikov, S. & Campagnola, P. J. Second harmonic generation microscopy for quantitative analysis of collagen fibrillar structure. *Nat. Protoc.* **7**, 654–669 (2012).
28. Löfstedt, T., Brynolfsson, P., Askund, T., Nyholm, T. & Garpebring, A. Gray-level invariant Haralick texture features. *PLoS One* **14**, e0212110 (2019).
29. Liu, Y. et al. Fibrillar Collagen Quantification With Curvelet Transform Based Computational Methods. *Front Bioeng. Biotechnol.* **8**, 198 (2020).
30. Dhomen, N. et al. Oncogenic Braf Induces Melanocyte Senescence and Melanoma in Mice. *Cancer Cell* **15**, 294–303 (2009).
31. Maiques, O. et al. A preclinical pipeline to evaluate migrastatics as therapeutic agents in metastatic melanoma. *Br. J. Cancer* **125**, 699–713 (2021).
32. Maiques, O. & Sanz-Moreno, V. Multiplex chromogenic immunohistochemistry to stain and analyze paraffin tissue sections from the mouse or human. *STAR Protoc* **3**, 101879 (2022).
33. Shellard, A. & Mayor, R. Collective durotaxis along a self-generated stiffness gradient in vivo. *Nature* **600**, 690–694 (2021).
34. Samuel, M. S. et al. Actomyosin-mediated cellular tension drives increased tissue stiffness and  $\beta$ -catenin activation to induce epidermal hyperplasia and tumor growth. *Cancer Cell* **19**, 776–791 (2011).
35. Fraley, S. I. et al. Three-dimensional matrix fiber alignment modulates cell migration and MT1-MMP utility by spatially and temporally directing protrusions. *Sci. Rep.* **5**, 14580 (2015).
36. Nerger, B. A., Brun, P. T. & Nelson, C. M. Marangoni flows drive the alignment of fibrillar cell-laden hydrogels. *Sci. Adv.* **6**, eaaz7748 (2020).
37. Doyle, A. D., Carvajal, N., Jin, A., Matsumoto, K. & Yamada, K. M. Local 3D matrix microenvironment regulates cell migration through spatiotemporal dynamics of contractility-dependent adhesions. *Nat. Commun.* **6**, 8720 (2015).
38. Grashoff, C. et al. Measuring mechanical tension across vinculin reveals regulation of focal adhesion dynamics. *Nature* **466**, 263–266 (2010).
39. Steinwachs, J. et al. Three-dimensional force microscopy of cells in biopolymer networks. *Nat. Methods* **13**, 171–176 (2016).
40. Dumbauld, D. W. et al. How vinculin regulates force transmission. *Proc. Natl. Acad. Sci. USA* **110**, 9788–9793 (2013).
41. Guilly, C. et al. The Rho GEFs LARG and GEF-H1 regulate the mechanical response to force on integrins. *Nat. Cell Biol.* **13**, 722–727 (2011).
42. Collins, C. et al. Localized tensional forces on PECAM-1 elicit a global mechanotransduction response via the integrin-RhoA pathway. *Curr. Biol.* **22**, 2087–2094 (2012).
43. Reuther, G. W. et al. Leukemia-associated Rho guanine nucleotide exchange factor, a Dbl family protein found mutated in leukemia, causes transformation by activation of RhoA. *J. Biol. Chem.* **276**, 27145–27151 (2001).
44. Lessey-Morillon, E. C. et al. The RhoA guanine nucleotide exchange factor, LARG, mediates ICAM-1-dependent mechanotransduction in endothelial cells to stimulate transendothelial migration. *J. Immunol.* **192**, 3390–3398 (2014).
45. Fares, J., Fares, M. Y., Khachfe, H. H., Salhab, H. A. & Fares, Y. Molecular principles of metastasis: a hallmark of cancer revisited. *Signal Transduct. Target. Ther.* **5**, 1–17 (2020).
46. Miskolczi, Z. et al. Collagen abundance controls melanoma phenotypes through lineage-specific microenvironment sensing. *Oncogene* <https://doi.org/10.1038/s41388-018-0209-0> (2018).
47. Pearce, O. M. T. et al. Deconstruction of a Metastatic Tumor Microenvironment Reveals a Common Matrix Response in Human Cancers. *Cancer Discov.* **8**, 304–319 (2018).
48. Barbazan, J. et al. Cancer-associated fibroblasts actively compress cancer cells and modulate mechanotransduction. *Nat. Commun.* **14**, 1–17 (2023).

49. Elosegui-Artola, A. et al. Matrix viscoelasticity controls spatio-temporal tissue organization. *Nat. Mater.* **22**, 117–127 (2022).
50. Stashko, C. et al. A convolutional neural network STIFMap reveals associations between stromal stiffness and EMT in breast cancer. *Nat. Commun.* **14**, 1–16 (2023).
51. Bera, K. et al. Extracellular fluid viscosity enhances cell migration and cancer dissemination. *Nature* **611**, 365–373 (2022).
52. Bansacal, N. et al. The extracellular matrix dictates regional competence for tumour initiation. *Nature* **623**, 828–835 (2023).
53. Fraley, S. I. et al. A distinctive role for focal adhesion proteins in three-dimensional cell motility. *Nat. Cell Biol.* **12**, 598–604 (2010).
54. Velez, D. O. et al. 3D collagen architecture regulates cell adhesion through degradability, thereby controlling metabolic and oxidative stress. *Integr. Biol. (Camb.)* **11**, 221–234 (2019).
55. Mistriotis, P. et al. Confinement hinders motility by inducing RhoA-mediated nuclear influx, volume expansion, and blebbing. *J. Cell Biol.* **218**, 4093–4111 (2019).
56. Law, R. A. et al. Cytokinesis machinery promotes cell dissociation from collectively migrating strands in confinement. *Sci. Adv.* **9**, eabq6480 (2023).
57. Orgaz, J. L. et al. Diverse matrix metalloproteinase functions regulate cancer amoeboid migration. *Nat. Commun.* **5**, 4255 (2014).
58. Georgouli, M. et al. Regional Activation of Myosin II in Cancer Cells Drives Tumor Progression via a Secretory Cross-Talk with the Immune Microenvironment. *Cell* **176**, 757–774.e23 (2019).
59. Alfert, A., Moreno, N. & Kerl, K. The BAF complex in development and disease. *Epigenetics Chromatin* **12**, 1–15 (2019).
60. Wu, J. N. & Roberts, C. W. M. ARID1A mutations in cancer: another epigenetic tumor suppressor? *Cancer Discov.* **3**, 35–43 (2013).
61. Cambria, E. et al. Linking cell mechanical memory and cancer metastasis. *Nat. Rev. Cancer* **24**, 216–228 (2024).
62. Saatci, O. et al. Targeting lysyl oxidase (LOX) overcomes chemotherapy resistance in triple negative breast cancer. *Nat. Commun.* **11**, 1–17 (2020).
63. Chitty, J. L. et al. A first-in-class pan-lysyl oxidase inhibitor impairs stromal remodeling and enhances gemcitabine response and survival in pancreatic cancer. *Nat. Cancer* **4**, 1326–1344 (2023).
64. Yao, Y. et al. Pan-Lysyl Oxidase Inhibitor PXS-5505 Ameliorates Multiple-Organ Fibrosis by Inhibiting Collagen Crosslinks in Rodent Models of Systemic Sclerosis. *Int. J. Mol. Sci.* **23**, 5533 (2022).
65. Shawk, A. M., Almalki, F. A., Abdalla, A. N., Abdelazeem, A. H. & Gouda, A. M. A Comprehensive Overview of Globally Approved JAK Inhibitors. *Pharmaceutics* **14**, 1001 (2022).
66. Acton, S. E. et al. Dendritic cells control fibroblastic reticular network tension and lymph node expansion. *Nature* **514**, 498–502 (2014).
67. Weigert, M. & Schmidt, U. NUCLEI INSTANCE SEGMENTATION AND CLASSIFICATION IN HISTOPATHOLOGY IMAGES WITH STARDIST. <https://doi.org/10.1109/ISBIC56247.2022.9854534> (2022).
68. Gentleman, R. C. et al. Bioconductor: open software development for computational biology and bioinformatics. *Genome Biol.* **5**, R80 (2004).
69. Gautier, L., Cope, L., Bolstad, B. M. & Irizarry, R. A. affy-analysis of Affymetrix GeneChip data at the probe level. *Bioinformatics* **20**, 307–315 (2004).
70. G, B. et al. ClueGO: a Cytoscape plug-in to decipher functionally grouped gene ontology and pathway annotation networks. *Bioinformatics* **25**, 1091–1093 (2009).
71. M, R. et al. GenePattern 2.0. *Nat. Genet.* **38**, 500–501 (2006).
72. Crescioli, S. et al. B cell profiles, antibody repertoire and reactivity reveal dysregulated responses with autoimmune features in melanoma. *Nat. Commun.* **14**, 1–21 (2023).
73. Satija, R., Farrell, J. A., Gennert, D., Schier, A. F. & Regev, A. Spatial reconstruction of single-cell gene expression data. *Nat. Biotechnol.* **33**, 495–502 (2015).
74. Weinstein, J. N. et al. The Cancer Genome Atlas Pan-Cancer analysis project. *Nat. Genet.* **45**, 1113–1120 (2013).
75. Curtis, C. et al. The genomic and transcriptomic architecture of 2,000 breast tumours reveals novel subgroups. *Nature* **486**, 346–352 (2012).

## Acknowledgements

VSM lab was supported by: the Institute of Cancer Research; Cancer Research UK (CRUK) C33043/A24478; Breast Cancer Now as part of Programme Funding to the Breast Cancer Now Toby Robins Research Centre; Barts Charity; Worldwide Cancer Research 22-0329 and UKRI grant reference EP/X033392/, Fundacion Alfonso Martin Escudero and by Marie Skłodowska-Curie Action (H2020-MSCA-IF-2014-EF-ST) and King's Overseas Scholarship. GOF's lab was supported by Cancer Research UK [C48390/A21153]. BF was supported by a King's Health Partners' studentship to VSM and GOF. Instituto de Salud Carlos III (ISCIII) through the project "PI18/00573 and PI21/00294" (R.M.M. and A.M.) and co-funded by the European Union; CIBERONC CB16/12/0023 (R.M.M. and X.M.G.). Comunidad de Madrid Atracción de Talento Investigador 2019-T1/BMD-13642 (supported J.L.O.). Blood Cancer UK Project 19001 and Cancer Research UK Centre City of London Centre grant C7893/A26233 (M.C.S. and A.B.). This work was [funded/supported] by Barts Charity (MGU0504) (O.M.). Tumour samples were processed by IRBLleida (B.0000682) PT17/0015/0027 and PT20/00021 and HUB-ICO-IDIBELL (PT17/0015/0024) Biobanks integrated in "Xarxa de Bancs de Tumors de Catalunya sponsored by Pla Director Oncologia de Catalunya (XBTC)", and Biobank and Biomodels Platform ISCIII. Views expressed are those of the author(s) and not necessarily those of the NHS, the NIHR, or the Department of Health. We acknowledge, BCI-CMR Advanced Bio-Imaging Facility of QMUL and ICR light-microscopy Facility, Chelsea, for the use, help and advice with microscopes, Andrew Clear and Nadia Rahman from BCI-Pathology facility, for the support in tissue processing and advice in tissue staining, BCI-BSU Animal Facility, for the support with the animal studies, Dr. Mathieu-Benoit Voisin from William Harvey Research Institute, QMUL, for support with the SHG setup, and Brian Nerger currently at John A. Paulson School of Engineering and Applied Sciences (Harvard University, Cambridge, US) for the technical advice to perform alignment experiments. We thank I. Malanchi (The Francis Crick Institute) and Anne Claire Dupuis (independent researcher) for scientific discussions. The graphic representation in the figures were created using BioRender.com.

## Author contributions

V.S.-M. was principal investigator, designed the study, supervised experiments, performed some experiments and wrote the manuscript; O.M. designed the study, performed most experiments, and wrote the manuscript. M.C.S. performed in vitro and tissue analysis supervised by A.B. P.P. designed parts of the study and performed experiments; R.L. performed spatial transcriptomics and RNAseq analysis supervised by S.T. and S.K. A.V., E.C.-M., Y.L. V.G., Y.J.-G. J.L.O. performed in vitro experiments. I.R.-H., J.B. and S.H. performed bioinformatics analysis. Y.A. and C.C.R.-A. performed image analysis experiments. J.S. performed in vivo experiments. G.O.F. supervised in vivo experiments performed by B.F. O.C. performed AFM measurements supervised by A.E.-A. E.M.G. and J.A. performed zymography experiments supervised by C.G. Human tissue materials, trichomic, ethics approvals and relevant anonymized clinical information was provided by M.S., A.M., J.T., X.M.-G. R.M.M., P.R.C.I., F.W. and K.B. provided Imaging support.

## Competing interests

The authors declare no competing interests.



## Additional information

**Supplementary information** The online version contains supplementary material available at <https://doi.org/10.1038/s41467-025-56299-7>.

**Correspondence** and requests for materials should be addressed to Victoria Sanz-Moreno.

**Peer review information** *Nature Communications* thanks the anonymous reviewers for their contribution to the peer review of this work. A peer review file is available.

**Reprints and permissions information** is available at <http://www.nature.com/reprints>

**Publisher's note** Springer Nature remains neutral with regard to jurisdictional claims in published maps and institutional affiliations.

**Open Access** This article is licensed under a Creative Commons Attribution-NonCommercial-NoDerivatives 4.0 International License, which permits any non-commercial use, sharing, distribution and reproduction in any medium or format, as long as you give appropriate credit to the original author(s) and the source, provide a link to the Creative Commons licence, and indicate if you modified the licensed material. You do not have permission under this licence to share adapted material derived from this article or parts of it. The images or other third party material in this article are included in the article's Creative Commons licence, unless indicated otherwise in a credit line to the material. If material is not included in the article's Creative Commons licence and your intended use is not permitted by statutory regulation or exceeds the permitted use, you will need to obtain permission directly from the copyright holder. To view a copy of this licence, visit <http://creativecommons.org/licenses/by-nc-nd/4.0/>.

© The Author(s) 2025

<sup>1</sup>Cytoskeleton and metastasis Team, The Breast Cancer Now Toby Robins Research Centre Division of Breast Cancer Research, The Institute of Cancer Research, Chester Beatty Laboratories, London SW3 6JB, UK. <sup>2</sup>Centre for Tumour Microenvironment, Barts Cancer Institute, Queen Mary University of London, John Vane Science Building, Charterhouse Square, London EC1M 6BQ, UK. <sup>3</sup>Randall Division of Cell and Molecular Biophysics, King's College London, New Hunt's House, Guy's Campus, London SE1 1UL, UK. <sup>4</sup>Centre for Haemato-Oncology, Barts Cancer Institute, Queen Mary University of London, John Vane Science Building, Charterhouse Square, London EC1M 6BQ, UK. <sup>5</sup>St. John's Institute of Dermatology, School of Basic and Medical Biosciences, King's College London, SE1 9RT London, UK. <sup>6</sup>Department of Informatics, Faculty of Natural and Mathematical Sciences, King's College London, Bush House, London WC2B 4BG, UK. <sup>7</sup>Cell and Tissue Mechanobiology Laboratory, The Francis Crick Institute, London NW1 1AT, UK. <sup>8</sup>Department of Computer Science, City St George's, University of London, London, UK. <sup>9</sup>Comprehensive Cancer Centre, School of Cancer and Pharmaceutical Sciences, King's College London, London SE1 1UL, UK. <sup>10</sup>CMR Advanced Bio-imaging Facility, Centre for Microvascular Research, Queen Mary University of London, John Vane Science Building, Charterhouse Square, London EC1M 6BQ, UK. <sup>11</sup>University Cote d'Azur, CNRS UMR7284, INSERM U1081, Institute for Research on Cancer and Aging, Nice (IRCAN), Nice, France. <sup>12</sup>Department of Pathology and Molecular Genetics, Hospital Universitari Arnau de Vilanova, University of Lleida, IRBLleida, CIBERONC, Lleida 25198, Spain. <sup>13</sup>Oncologic Pathology Group, IRBLleida, Departments of Experimental Medicine and Basic Medical Sciences, University of Lleida, Lleida 25198, Spain. <sup>14</sup>Department of Pathology, Hospital Universitari de Bellvitge University of Barcelona, IDIBELL, CIBERONC, L'Hospitalet, Barcelona 08907, Spain. <sup>15</sup>Department of Dermatology, Hospital Universitari Arnau de Vilanova, CIBERONC, University of Lleida, CIBERONC, IRB Lleida, Lleida 25198, Spain. <sup>16</sup>Instituto de Investigaciones Biomédicas Sols-Morreale (IIBM), CSIC-UAM, 28029 Madrid, Spain. <sup>17</sup>Quell Therapeutics, Translation & Innovation Hub, 84 Wood Ln, London W12 0BZ, UK. <sup>18</sup>Light Microscopy Facility, The Institute of Cancer Research, Chester Beatty Laboratories, London SW3 6JB, UK. <sup>19</sup>Integrated Pathology Unit, Division of Molecular Pathology, The Institute of Cancer Research, Sutton, UK. <sup>20</sup>Breast Cancer Research Bioinformatics Group, Chester Beatty Laboratories, London SW3 6JB, UK. <sup>21</sup>Breast Cancer Now Research Unit, School of Cancer & Pharmaceutical Sciences, King's College London, Guy's Cancer Centre, London SE1 9RT, UK. <sup>22</sup>Present address: Cancer Biomarkers & Biotherapeutics, Barts Cancer Institute, Queen Mary University of London, London, UK. <sup>23</sup>These authors contributed equally: Marta C. Sallan, Roman Laddach, Pahini Pandya. ✉ e-mail: [victoria.sanz-moreno@icr.ac.uk](mailto:victoria.sanz-moreno@icr.ac.uk)